BOUNDS ON TERTIARY SHORTENING AT THE NORTHEASTERN MARGIN OF THE TIBETAN PLATEAU

Charles Angerman[1], Eric Kirby[1], Xuhua Shi[2], Marin Clark[3], and Ken Farley[4],

[1]Department of Geosciences, Penn State University, University Park, PA 16802
[2]Institute for Geology, Chinese Academy of Sciences, Beijing, P.R. China
[3]Department of Geological Sciences, University of Michigan, Ann Arbor, MI 48109
[4]Division of Geological and Planetary Sciences, Caltech, Pasadena, CA 91125

Manuscript for submission to *Tectonics*, February 3, 2007

ABSTRACT

Quantifying the magnitude and spatial extent of Tertiary deformation in the Indo-Asian collision zone is central to a deeper understanding of the growth of the Tibetan Plateau in space and time, relative roles of crustal and mantle processes, and linkages between high elevation in central Asia and global climate. Here we characterize the style, magnitude and timing of shortening along a regionally-extensive thrust system in northeastern Tibet, the West Qinling fault. Mapping and structural analysis of Tertiary sediments preserved in the hanging wall of this thrust allows reconstruction of shortening at a tip-line fold near the eastern edge of the Linxia basin. Restoration of balanced cross-sections indicates limited shortening (1-3 km) across the fault. Moreover, geomorphic observations reveal a contiguous, low-relief erosional landscape south of the fault system that truncates structures on the plateau and restricts deformation to pre-Tertiary. The southern boundary of this low-relief surface is defined by a south-vergent thrust system along the margin of the Lintan basin; preliminary estimates of shortening across this fault appear to be less than ~5 km. (U-Th)/He thermochronology of apatite from the hanging wall of the West Qinling fault reveal slow denudation rates (~20 m/m.y.) during Paleocene – Miocene time and suggest that slip on the fault, and development of relief along the range front, occurred subsequent to ~20 Ma. Overall, our results reveal minimal shortening of the upper crust during Late Cenozoic development of the northeastern Tibetan Plateau and provide support for models invoking redistribution of crust by ductile flow.

1. INTRODUCTION

The question of how and when the Tibetan Plateau attained its current elevation remains a first-order problem in continental tectonics, carrying implications for the processes of intracontinental deformation [c.f., *England and Houseman*, 1986; *Royden*, 1996; *Tapponnier, et al.*, 1982], the linkages between plateau growth and climate change [*Molnar, et al.*, 1993], and the role of mantle processes in plateau development [e.g., *Garzione, et al.*, 2006]. Although there is a general consensus that the plateau grew in lateral extent as a consequence of crustal thickening driven by the continuing convergence of India and Eurasia [*Argand*, 1924; *England and Houseman*, 1986; *Royden*, 1996; *Tapponnier, et al.*, 2001; *Zhao and Morgan*, 1985], our understanding of the progression of deformation in time and space remains skeletal at best. Important uncertainties regarding the magnitude of pre-collision shortening and inferred crustal thickness within the present plateau [e.g., *Kapp, et al.*, 2003a; *Kapp, et al.*, 2005; *Kapp, et al.*, 2003b; *Murphy, et al.*, 1997], the elevation history of different regions of the plateau [*Currie, et al.*, 2005; *Rowley and Currie*, 2006], coupled with an incomplete knowledge of the distribution and magnitude of Tertiary shortening in the crust [c.f., *Yin and Harrison*, 2000] and a limited understanding of the evolution of mantle buoyancy through time [*Molnar, et al.*, 1993], continue to drive debate over the processes of intracontinental deformation in this archetypal orogen.

Central to this debate is the mechanism of crustal thickening itself, for which two end-member hypotheses exist. In the first case, plateau growth is achieved through large-magnitude shortening and contractional deformation of the upper crust along major basin-bounding fault systems. Such models point to large-magnitude deformation observed in Tertiary sediments within the plateau [*Horton, et al.*, 2002; *Murphy and Yin*, 2003; *Yin, et al.*, 1999] and near its margins [*Fang, et al.*, 2003; *Ritts, et al.*, 2004] as evidence for shortening in the upper crust.

Moreover, a broad northward progression in the timing of deformation has led to the suggestion that the plateau underwent a punctuated history of outward growth characterized by large-scale continental subduction of lithospheric blocks [*Tapponnier, et al.*, 2001]. In contrast, a second class of models considers the plateau to have grown outward primarily by lateral flow of isostatically-compensated weak lower crust [*Royden*, 1996]. Such models point to an apparent absence of significant contractional structures in eastern Tibet [*Burchfiel, et al.*, 1995; *Kirby, et al.*, 2000; *Royden, et al.*, 1997] and the preservation over long wavelengths of a regionally-extensive low-relief surface at high elevation in southeastern Tibet [*Clark and Royden*, 2000; *Clark, et al.*, 2006]. Such models can be highly sensitive to the surface boundary condition at plateau margins [*Beaumont, et al.*, 2001], and a wide range of behavior may result as a consequence of various degrees of coupling between the lower and upper crust. Deconvolving the relative roles of upper crustal shortening versus lower crustal flow during growth of the Tibetan Plateau remains challenging.

The northeastern corner of the Tibetan Plateau represents one region that provides an opportunity to quantitatively assess the contribution of Tertiary upper crustal shortening to the present-day crustal thickness (Figure 1). In contrast to the relatively low internal relief on the central and eastern plateau, northern Tibet is characterized by high-standing ranges and intervening basins (Figure 1). Geodetic [*Zhang, et al.*, 2004] and geologic [*Peltzer, et al.*, 1988; *Van der Woerd, et al.*, 2001] studies attest to active shortening of the upper crust within the Qilian Shan and associated ranges. Although the timing of onset of deformation is the subject of some debate [c.f., *Métivier, et al.*, 1998; *Yin, et al.*, 2002], it is clear that significant Tertiary shortening of the upper crust contributes to the development of high topography [*Burchfiel, et al.*, 1989; *Meyer, et al.*, 1998; *Tapponnier, et al.*, 1990]. To the east, however, in the vicinity of

Xining and Lanzhou (Figure 1) the topography becomes transitional with that of the eastern Tibetan Plateau (Figure 1). The plateau in this region is characterized by high elevations (~3500 – 4000 m) and relatively subdued local relief; Clark and Royden [2000] interpreted the smooth, long-wavelength decrease in elevation from SW to NE across this region as reflecting thickening by influx of lower crust. However, several large Tertiary basins exist in the region (Figure 1), the largest of which, the Linxia Basin, has been interpreted to have been deposited in a flexural foredeep during Tertiary shortening along a regionally-extensive thrust system [*Fang, et al.*, 2003]. Thus, this region possesses topographic and structural characteristics that are perhaps indicative of both upper crustal shortening and lower crustal flow.

In order to better understand the relative contribution of these processes to growth of high topography in northeastern Tibet, we seek to quantify the amount of Tertiary shortening recorded in the upper crust at the margin of the Linxia Basin (Figure 1) and assess the contribution of this shortening to the present-day thickness of the crust. Along the Tao River, Neogene sediments of the Linxia Basin are preserved in the hanging wall of the West Qinling thrust system, a major, north-vergent fault system that bounds the southern margin of the Linxia Basin. Mapping and stratigraphic study of these sediments allow quantitative reconstruction of the magnitude of Tertiary deformation along the fault system. Moreover, regionally-extensive geomorphic surfaces in the hanging wall of the fault system place limits on the amount of deformation within the plateau south of the basin-bounding fault. These results, in conjunction with low-temperature thermochronometric data from hanging wall rocks, suggest that most of the deformation observed throughout this region of the plateau is pre-Cenozoic in age, and does not contribute to the budget of Tertiary shortening.

2. GEOLOGIC SETTING

2.1. Late Tertiary Deformation in Eastern Tibet

The geologic and topographic evolution of the eastern and southeastern regions of the Tibetan Plateau has served to cultivate the proposition that flow of weak lower crust can drive crustal thickening in the absence of significant shortening of the upper crust [e.g., *Royden*, 1996]. The primary lines of evidence for such a mechanism operating in eastern Tibet include the following: 1) slow rates of present-day shortening across the steep margin of the plateau against the Sichuan Basin [*King, et al.*, 1997]; 2) limited Cenozoic shortening across this margin [*Burchfiel, et al.*, 1995] and the absence of a Cenozoic foredeep in the Sichuan Basin [*Royden, et al.*, 1997]; 3) long-wavelength, low-gradient topographic margins of the plateau in southeastern and northeastern Tibet [*Clark and Royden*, 2000]; 4) rapid deformation and tilting of markers in eastern Tibet, despite limited horizontal shortening [*Kirby, et al.*, 2000]; and 5) preservation of a low-relief landscape at high elevation in southeastern Tibet that appears to have once been continuous across southeastern China [*Clark, et al.*, 2006; *Schoenbohm, et al.*, 2004].

Our present understanding of the timing of plateau development in eastern and southeastern Tibet relies largely on rapid cooling inferred from thermochronologic proxies. Disruption of the low-relief surface atop the plateau by fluvial incision appears to have begun in the late Miocene [*Clark, et al.*, 2005a; *Kirby, et al.*, 2002]. Importantly, (U-Th)/He ages from apatites on or near preserved remnants of low-relief surfaces yield Mesozoic ages [*Clark, et al.*, 2005a; *Xu and Kamp*, 2000], consistent with thermal histories from the Sichuan Basin margin suggesting very slow rates of cooling and denudation since Mesozoic time [*Kirby, et al.*, 2002]. Thus, throughout much of eastern Tibet, remnant patches of a low-relief, relict landscape appear to pre-date the Late Cenozoic development of high topography and rugged relief [e.g., *Clark, et al.*, 2006].

2.2. Tertiary Deformation and Basin Development in Northeastern Tibet

In contrast to the eastern and southeastern regions of the Tibetan Plateau, where little evidence exists for deformation of the upper crust, the northeastern margin is characterized by a series of large Tertiary basins, bounded by thrust systems (Figure 1). The largest of these, the Linxia Basin, lies to the north and east of high ranges in the West Qinling and La Jie Shan (Figure 1) and is bound on the south by a north-vergent thrust system, herein referred to as the West Qinling thrust. In addition, numerous small Tertiary basins sit today at high elevations (>3000 m) within the Tibetan Plateau to the south (Figure 1). The largest of these, the Lintan Basin, is bounded along its northern margin by a south-vergent thrust system (Figure 1). The association of terrestrial basins and range-bounding thrust faults in northeastern Tibet has led a number of workers to the conclusion that sediment accumulation was driven by subsidence associated with shortening [*Fang, et al.*, 2003].

The timing of fault activity in the region, however, remains the subject of debate. This part of northeastern Tibet has been the locus of terrestrial sediment accumulation since the Late Jurassic – Early Cretaceous. Horton et al. [2004] suggested that Mesozoic sediments accumulated during transtensional basin formation and subsequent thermal subsidence. These workers observe a clockwise rotation of paleomagnetic poles [*Dupont-Nivet, et al.*, 2004], coincident with an increase in sediment accumulation rate in the mid-Tertiary from which they infer that shortening related to the Indo-Asian collision initiated in northeastern Tibet as early as 40-30 Ma.

A similar conclusion was reached from stratigraphic studies in the Linxia basin (Figure 1). Fluvial and lacustrine sediments of the Linxia basin were deposited between 29 Ma and ~1.7 Ma, based on magnetostratigraphic and biostratigraphic correlation of three stratigraphic sections with the geomagnetic polarity reversal timescale [*Fang, et al.*, 2003]. There is some debate over the exact biostratigraphic age of the lowermost units of the basin stratigraphy; Deng et al. [2004] reevaluated fossils from Linxia basin sediments and suggested that the base of the section studied by Fang et al. [2003] may be up to ~7 m.y. older. Although the details remain uncertain, it appears that the onset of Tertiary sediment accumulation occurred between ~36 and ~29 Ma. Based on regional stratigraphic correlations, these workers suggested that sedimentation took place in a flexural foreland basin and inferred that shortening on the basin-bounding fault was activated during the late Oligocene.

There are a number of regional studies, however, that document a coordinated pulse of tectonic activity across northeastern Tibet in the Late Miocene [*Molnar*, 2005]. In the Linxia basin, sediment accumulation rates increased during the mid-late Miocene (ca. 12 Ma) [*Fang, et al.*, 2003]. This event appears to coincide with a shift toward less negative $\delta^{18}O$ values of lacustrine and soil carbonates in the basin sediments [*Dettman, et al.*, 2003], which the authors suggest may herald the onset of more arid conditions in northeastern Tibet, a possible consequence of blocking of incoming moisture associated with the East Asian monsoon. It also coincides with a change in the isotopic (ε_{Nd}) values mudstones from the basin [*Garzione, et al.*, 2005], consistent with an increase in exhumation rate of Mesozoic and Paleozoic source rocks exposed south of the Linxia basin. Perhaps not coincidentally, cooling rates in the hanging wall of the West Qinling fault, along the Daxia River (Figure 1), are inferred to have increased around this time [*Clark, et al.*, 2004]. Finally, a decrease in the lag time between fission-track ages of detrital apatite samples and their depositional age occurs at ca. 12-14 Ma [*Zheng, et al.*, 2003] and may reflect an increase in exhumation rate of the basin-bounding ranges. Regionally, the Late Miocene also marks the emergence of the La Jie Shan as a sediment source to the Guide basin [ca. 8 Ma, *Lease, et al.*, in press] and is a time of rapid cooling and exhumation in ranges north and east of the Linxia Basin [*Enkelmann, et al.*, 2006; *Zheng, et al.*, 2006].

Despite the wealth of stratigraphic and paleoenvironmental data from the center of the Linxia basin, little is known about the style, magnitude, or rates of deformation along the basin margins. The basin is bounded on its southern margin by a regionally-extensive, north-vergent thrust fault, the West Qinling fault system (Figure 1) that places Paleozoic and Mesozoic rocks over Linxia basin sediments. This system extends over ~250 km along strike, forming the southern boundary of the Xun Hua and Guide basins west of the Linxia region. Although the Xun Hua basin is not as well-studied as Linxia, sediment accumulation in the Guide basin extends back to at least the mid-Miocene [*Fang, et al.*, 2005; *Pares, et al.*, 2003]. East of the Linxia basin, the West Qinling fault system is not as well exposed, but has been suggested to continue eastward for at least ~100 km [Tianshui/Gansu fault of *Horton, et al.*, 2004], along the southern margin of the Longxi basin (Figure 1). In this region, the West Qinling fault system is overprinted by active, left-lateral faults of the Wei He graben system [*Peltzer, et al.*, 1985] that obscure much of the older history. Regardless, the West Qinling fault system represents a regionally-significant shortening structure whose role in the tectonic evolution of northeastern Tibet is only poorly understood. The primary goal of this paper is to characterize the timing and magnitude of shortening accomplished by slip on this fault system.

3. GEOLOGY AND GEOMORPHOLOGY OF THE WEST QINLING RANGE

The Tibetan Plateau south of the Linxia Basin exhibits mean elevations between ~3500 and 4000 m, with peaks in the West Qinling range reaching elevations of over 4500 m (Figure 2). Local relief on the range front against the Linxia basin today approaches 2000 m. The range itself is drained by two major tributaries of the Yellow River, the Daxia and Tao rivers (Figure 1), both of which have carved deep gorges into the plateau surface (Figure 2). However, between these rivers, and south of the West Qinling proper, the plateau is characterized by subdued local relief and low topographic gradients (Figure 2).

To better characterize the geometry and extent of this low-relief surface atop the plateau in this region, we analyzed digital topographic data from the Shuttle Radar Topography Mission (SRTM, 3-arc second resolution; http://srtm.csi.cgiar.org/). Visualization of the gradient of the land surface reveals steep slopes on the plateau, especially in areas adjacent to major rivers and at the West Qinling range front (Figure 2). However, several large regions of contiguous low gradient are apparent south of the West Qinling (Figure 2b). Utilizing a combination of gradient and curvature (Laplacian of topographic surface, or $\nabla^2 z$) [*Zevenbergen and Throne*, 1987], we delineate the regional extent of low-relief surfaces at the northeastern plateau margin (Figure 2c). Comparison of this result with the geology of the region [*Ministry of Geology and Mineral Resources*, 1989; 1991] reveals that many of the low-relief surfaces are mantled by Tertiary and Quaternary sediments (e.g., Hezuo, Ganjia, and Sangke basins, Figure 2d), but two major surfaces are apparently devoid of Cenozoic sediments. One of these (referred to locally as the Meiwu plateau) lies immediately south of the Linxia Basin, extends for ~60 km E-W and nearly 40 km N-S, and is bounded on the north and south by higher topography at the margins of the Linxia and Lintan basins (Figure 2).

The character of the Meiwu surface is similar to low-relief landscapes observed atop the Tibetan Plateau in eastern and southeastern Tibet [*Clark, et al.*, 2005a; *Clark, et al.*, 2006; *Kirby, et al.*, 2002]. Of particular note is the observation that Neogene sediments in the vicinity of the Tao river (Figure 2d) ramp up onto the Meiwu surface at its eastern end, and remnant patches of sediment are mapped atop the surface at its southwestern corner (Figure 3). This apparent onlap of Neogene sediments indicates that the surface likely represents a relict landscape that existed prior to Tertiary basin development. As we document below, Neogene sediments that onlap the eastern margin of the Meiwu plateau are continuous with sediments in the Linxia basin proper. Thus, the surface appears correlative with the basal unconformity beneath Neogene sediments in the Linxia basin and can be used as an additional constraint on the magnitude of Tertiary deformation across this region of the plateau.

3.1. Geology in the Tao He region

Along much of the exposed margin of the Linxia basin, a lack of hanging-wall cutoffs precludes a precise estimate of shortening across the West Qinling fault zone (Figure 3). Near the eastern end of the basin, however, in the vicinity of the Tao He (river), Neogene sediments extend across the fault into the West Qinling range. The presence of sediments in both the hanging wall and footwall blocks allows us to use the basal unconformity as a marker that allows reconstruction of shortening across this portion of the fault system.

To better constrain the geometry and distribution of deformation associated with the West Qinling fault system, we undertook geologic mapping along the fault between the Daxia and Tao rivers (Figure 1). Our efforts focused on macroscopic structures near the eastern end of this region, but also include reconnaissance observations at exposures of the range-bounding fault. We combined these observations with published geologic maps [*Ministry of Geology and*

Mineral Resources, 1989] of the Carboniferous through Triassic bedrock in the West Qinling and on the plateau south of the Linxia basin. We briefly describe the geologic units found in the region, before characterizing the geometry and extent of Tertiary deformation recorded in them.

3.1.1. Paleozoic and Triassic Units. Paleozoic and Mesozoic strata are exposed within a regionally-extensive anticlinal culmination along the West Qinling south of the Linxia basin (Figure 3). The anticlinorium extends ~170 km along strike, exposing Carboniferous through Permian strata in the core and Triassic units along the limbs of the structure (Figure 3). Where we had the opportunity to observe them, Carboniferous and Permian rocks are typically massively-bedded, gray to blue-grey carbonates with subordinate interlayers of shale and fine sandstone. These units constitute a portion of the eastern Kunlun-Qaidam terrane [*Yin and Harrison*, 2000] and record widespread shallow marine conditions during the Carboniferous. Rare exposures of latest Permian strata reveal a transition to coarser lithologies dominated by siliclastic components. Upper Permian strata are gradational with Triassic strata of the Songpan-Ganzi flysch complex [*Sengör and Natal'in*, 1996; *Yin and Harrison*, 2000], and the onset of siliclastic accumulation has been interpreted to record the incipient collision between North and South China in latest Permian time [*Chang*, 2000].

Triassic rocks near the Linxia basin margin consist of interbedded sandstones and argillaceous shales; sandstones are commonly feldspathic or lithic-rich wackes. These rocks represent some of the northernmost exposures of the Songpan-Ganzi flysch, a volumetrically extensive package of deep-marine turbidite deposits [*Sengör and Natal'in*, 1996; *Yin and Harrison*, 2000] shed off the rising Qinling-Dabie orogen [*Bruguier, et al.*, 1997; *Chang*, 2000; *Zhou and Graham*, 1996].

Paleozoic and Mesozoic strata in the field site were intruded by several intermediate to felsic plutons designated as Jurassic in age [*Ministry of Geology and Mineral Resources*, 1989]. Plutonic rocks appear to cross-cut structures and fabrics within the Paleozoic sequence (Figure 3), suggesting that they were emplaced late in the deformational history. Rare exposures of Jurassic volcanics are present near the western extent of the Meiwu surface (Figure 3).

3.1.2. Cretaceous Sedimentary Units. Terrestrial siliciclastic sedimentary rocks designated as Cretaceous [*Ministry of Geology and Mineral Resources*, 1989] are exposed north and east of the Tao He (Figure 4) and consist primarily of interbedded sandstones and mudstones, with minor lenses of pebble conglomerate. Mudstones are typically purple-brown in color with numerous reduction spots and exhibit planar, laminated bedding on centimeter-scales, whereas sandstone interbeds are present in sets ranging from 30 cm to 2 m thick with planar cross-beds. Conglomerates consist of matrix-supported granule-cobble conglomerates with clasts up to 10 cm in diameter. Clast compositions are primarily limestone and quartzite, with rare occurrences of plutonic or metamorphic rocks and appear to reflect a source region similar to that exposed today in the West Qinling.

Terrestrial sedimentary rocks at the northeastern plateau margin have been designated as Cretaceous in age on the basis of fossil assemblages and magnetostratigraphy in the Xining-Minhe Basin [e.g., *Hao*, 1988; *Horton, et al.*, 2004]. In the Linxia region, units are designated as Cretaceous on the basis of fossils of *Sinamia sp.*, a freshwater fish of the Upper Jurassic-Lower Cretaceous in east Asia, and gingko and cycad pollen [*Ministry of Geology and Mineral Resources*, 1989].

Cretaceous sediments at the southern edge of the Linxia basin appear to represent deposition in a terrestrial setting dominated by fluvial and floodplain environments. Mudstones and very fine sandstones likely result from deposition during crevasse splay events, while fluvial sands and gravels are attributable to sedimentation within channels. Near the contact with Triassic bedrock, some of the coarser units may represent higher-energy deposits associated with braided river and/or alluvial fan settings. Lithologically, these units are similar to Cretaceous units in the Maxian Shan, near Lanzhou (Figure 1) and appear to represent southeastern exposures of the Xining-Minhe basin [*Horton, et al.*, 2004]. Regional fining of Cretaceous conglomerates toward the northeast and provenance suggest that the present-day margin of the Linxia basin was coincident with the paleo-margin of the Cretaceous-Paleogene Xining-Minhe basin [*Horton, et al.*, 2004].

3.1.3. Tertiary basin deposits. Tertiary deposits at the margin of the Linxia basin in the vicinity of the Tao He are considered to be Neogene in age [*Ministry of Geology and Mineral Resources*, 1989]; therefore, throughout the paper, we refer to them as such. However, direct biostratigraphic or radiometric control is sparse. A consideration of relative age constraints is presented below. As described below, lithologic similarities to Tertiary strata in the center of the basin, clast provenance, and unconformable relationships with Cretaceous units all suggest a Tertiary age.

Tertiary deposits south of the Linxia basin margin consist primarily of coarse pebble to boulder conglomerate with interbedded sandstones and mudstones. Grain sizes within these units fine rapidly northward away from the West Qinling, and exposures throughout the majority of the basin are fine mudstone and siltstone. Conglomerates are generally matrix-supported, though the degree of matrix varies widely. Clasts range in size from granule to boulder, but are typically subrounded pebbles and cobbles (up to 10-15 cm). Most conglomerate clasts are sandstone and/or limestone, with minor quartzite, and appear to be derived from Paleozoic and Mesozoic units to the south. Rare clasts of granite or diorite can be found in the southern parts of the basin. Typically, conglomerates are massively bedded (1-3 m) and support cliffs many 10s of meters high (Figure 5b – see photo). Interbedded with these deposits are finer-grained units, ranging from sandstone to mudstone. Sandstones are present in packages of laterally continuous beds 30 cm to 1 m thick with planar laminations and subordinate cross-beds. Associated mudstones typically range in grain size from very fine sand to coarse silt, are thinly laminated, and often exhibit gradational contacts with coarser sands.

Tertiary strata near the range front appear to represent both high-energy fluvial and alluvial fan deposits. Sandstones and most conglomerates appear to reflect deposition in a proximal fluvial environment, though the presence of some coarse, angular, clast-supported conglomerates suggests local deposition by hyperconcentrated flow in alluvial fans. Rare fine-grained sandstones and mudstones are interpreted to represent overbank deposits. Of particular importance is the fact that conglomerates extend across the frontal fold at the eastern end of the basin-bounding fault (Figure 4) and rapidly grade northward into finer sediments in the Linxia basin. The continuity of units across the projected trace of the West Qinling fault system has important consequences for the geometry and magnitude of deformation (discussed below).

Tertiary units are distinct from Cretaceous rocks on the basis of several field observations. Where both units are in proximity to one another, in the northeastern portion of the study area (Figure 4), Tertiary rocks lie unconformably atop Cretaceous rocks and contain an abundance of clasts (1-5 cm) of the underlying Cretaceous mudstone and shale, indicating a younger relative age. Second, Cretaceous units tend to exhibit a greater degree of induration and possess a characteristic joint set orthogonal to bedding that is absent in Tertiary deposits. Finally, south of the basin margin, Tertiary conglomerates generally exhibit a bright red matrix whereas Cretaceous conglomerates are grayish tan to brown in color. These differences, although qualitative, indicate that Tertiary deposits are recognizable and distinct from Cretaceous strata. Moreover, the presence of Cretaceous clasts within the Tertiary basin deposits suggests they must be of Tertiary age.

Although the distance to the sections studied by Fang et al. [2003] near the center of the Linxia basin precludes direct lithostratigraphic correlation to dated strata, the presence of Tertiary conglomerates atop a basal unconformity with Paleozoic bedrock suggests that these deposits are likely correlative with the lower portions of the Linxia basin section. In the basin center, the Tala Formation lies unconformably on granite bedrock and has been dated at 29-21.4 Ma [*Fang, et al.*, 2003]. The Tala formation and overlying Zhongzhuang formation, dated at 21.4-14.7 Ma, are the only pre-late Miocene units in the Linxia basin that contain coarse conglomerate beds [*Fang, et al.*, 2003]. Thus, it seems probable that Tertiary deposits in the Tao He region are stratigraphically equivalent to the Tala Formation. However, difficulties in correlating terrestrial sedimentary units on the basis of lithostratigraphy and the likely time-transgressive nature of the basal Neogene unconformity make this correlation tentative. The deposits could be as old as Paleocene or as young as Miocene; a more precise determination awaits discovery of biostratigraphic or magnetostratigraphic markers.

3.1.4. Quaternary sediments. Abundant Quaternary sediments mantle Neogene deposits in the Linxia basin and the adjacent region of the Tibetan Plateau. Quaternary fluvial deposits are present along both the Tao and Daxia rivers. In addition, a thick (>30 m in some locations), extensive layer of Quaternary loess drapes Neogene sediments within the Linxia basin and represents the western portion of the Chinese loess plateau. Qualitative observations of fluvial terraces along the Tao and Daxia rivers suggest that terraces are not displaced or deformed across the basin-bounding fault, and these deposits are not discussed further.

3.2 Deformation recorded in Neogene deposits

Neogene conglomerates at the margin of the Linxia basin display varying amounts of deformation and serve as a marker for estimating Cenozoic shortening at the northeastern edge of the plateau. Along much of the southern margin of the basin, the West Qinling thrust places Permo-Triassic rocks on top of basin sediments (Figure 2). Although the fault plane is not well exposed, the geometry of the fault trace where it crosses several canyons between the Daxia He and Tao He (Figure 1) suggests that the fault dips moderately to steeply south (26°-48°; Table 1). Neogene sediments in the footwall of the fault are deformed into synclinal, upright folds immediately beneath the fault, but the lack of preserved hanging-wall cutoffs precludes reconstruction of fault slip along this portion of the fault system.

Eastward along the range front, however, the fault transitions into a range-scale ESE-trending anticline (Figure 4). On the north limb of the anticline, the basal unconformity between Neogene conglomerates and Permian bedrock in the range dips steeply northward. Beds immediately above the unconformity dip steeply north to northeast, and are locally overturned (Figure 5b – see photo). Bedding dips in the basin grade rapidly northward into gentle (<10°) orientations. South of the range front, in the valley of the Tao He, Neogene strata dip moderately southward (30°-35°) defining the backlimb of the fold. Overall, the anticline is a broad, asymmetric fold with a steep NNE-dipping forelimb and a gentle SSE-dipping backlimb (interlimb angle is ~100º). Stereonet analysis of the poles to Neogene bedding measurements from both limbs of the fold (Figure 4, inset) permits estimation of the trend and plunge of the fold axis. Attitude measurements on the limbs of the fold exhibit some scatter, but tend to cluster about a girdle. The pole to a best-fit plane through this distribution yields a fold axis trending 104º and plunging 18º SE.

A range-scale fold of this geometry is also consistent with the geometry of deformed Cretaceous strata east of the Tao He (Figure 4). Cretaceous units dip steeply (up to 60°) northward along the range front (Figure 5c – see photo); dips progressively decrease northward into the Linxia basin, where they are buried by Neogene deposits (Figure 4). Rare southward dips suggest the presence of minor synclines north of the range front (Figure 4), and a minor backthrust is present at the Cretaceous-Triassic contact (Figure 4 and 5). Overall, however, the geometry appears similar to the range-scale fold in Neogene sediments west of the Tao He, and suggests that the steep forelimb of the anticline continues eastward along the range front.

The along-strike transition from an emergent fault trace to a depositional contact suggests that the basin-bounding fault is blind beneath the Neogene sediments in the vicinity of the Tao He. The asymmetric form of the fold and the lateral continuity with a regionally-extensive thrust fault further suggest that the frontal anticline represents a leading-edge anticline above a propagating fault tip (Figure 5).

Subsidiary southeast-trending folds are present in the Neogene conglomerates to the south and west of the frontal fold (Figure 4). Sediments in these folds display somewhat gentler dips than the forelimb of the main frontal anticline and exhibit complex, minor, parasitic folds on their limbs (Figure 4). The overall structure, however, is indicative of SW-NE contraction across the basin margin.

3.3. Timing of deformation and sedimentation

The coarse character and sedimentary structures of Neogene deposits south of the Linxia Basin suggests deposition in a high-energy, proximal environment that was likely associated with relatively high local relief. Stratigraphic evidence for synchronous deformation and sedimentation, however, is somewhat equivocal on the limbs of the frontal anticline. The rapid decrease in bedding dip northward toward the Linxia basin (Figure 5) is consistent with some degree of fold growth during sediment accumulation, although a lack of exposure prevented definitive identification of progressive unconformities. Additionally, the abrupt transition along strike from a blind frontal thrust to an emergent structure may in part reflect changes in the depth of exposure of the basin fill. Again, however, incomplete exposure within basin sediments prevents lateral tracing of units along the front to test this hypothesis. On the backlimb of the anticline, conglomerates display a subtle decrease in dip upsection that may reflect progressive deformation of beds. However, the magnitude is small (from ~35° to ~25°) and lies within the range of measurement uncertainty in coarse terrestrial sedimentary rocks. Together, these observations permit the possibility that sedimentation and deformation were synchronous, but it is also possible that much of the sediment accumulation locally pre-dates fold development, perhaps as a consequence of rapid accumulation rates.

Paleoflow directions inferred from imbricated clasts within Neogene conglomerates in the hanging wall provide only limited evidence for synchronous deposition and local fold growth. Measurements of the attitudes of multiple imbricated clasts (backrotated to account for bedding dips) at 20 locations yielded down-current flow directions that show considerable scatter (Figure 6); however, there is a general trend of east-northeast flow, oblique to the anticlinal hinge in the southwestern portion of the basin (Figure 6). This trend is consistent with a sediment source farther to the south in the West Qinling. However, several sites suggest that locally flow was opposite to this trend and directed to the south, away from the Linxia Basin (Figure 6). These sites all occur on the flanks of anticlinal structures, and may reflect local sediment sources on structural and topographic highs. Paleoflow directions at these sites are consistent with synchronous deposition and local fold growth.

Finally, a comparison of bedding dips in Neogene rocks exposed on the forelimb of the anticline with deformation recorded in Cretaceous rocks provides a direct constraint on the relative timing of folding and deposition. Neogene and Cretaceous sediments along the present-day topographic margin exhibit similar degrees of deformation. Cretaceous units dip steeply (~60°) near the range front, immediately north of a minor, south-vergent reverse fault (Figure 4, 5c) and decrease to gentler dips farther north. This is quite similar to the pattern observed in Neogene sediments west of the Tao He, and suggests that both units have experienced similar amounts of shortening. Thus, we infer that folding of Neogene sediments in the Tao He region faithfully record the bulk of Tertiary shortening on the West Qinling fault system at this longitude.

4. RECONSTRUCTION OF SHORTENING IN NORTHEASTERN TIBET

The geometry of the frontal anticline near the Tao River and its association with the West Qinling thrust suggest that the basal Neogene unconformity is a suitable marker for reconstructing shortening across this fault system. Moreover, the presence of a low-relief erosion surface (Meiwu plateau) and Neogene deposits in the Lintan basin to the south enable a regional estimate for the magnitude of Tertiary shortening during development of this portion of the Tibetan Plateau. In this section, we utilize constraints imposed by these geologic relationships to facilitate the development of maximum and minimum bounds on the amount of Tertiary shortening.

4.1. Shortening across the margin of the Linxia Basin

The excess area balancing method [*Mitra and Namson*, 1989] allows restoration of deformation at the southern edge of the Linxia basin. Models presented here share an assumption of a subhorizontal pre-depositional topography. We recognize that this was probably not strictly true, but it is consistent with the relatively low-relief Meiwu surface. We utilize the geometry of the deformed Neogene sediments as representative of the geometry of the deformed unconformity. We focus on the frontal anticline and model it as a fault-propagation fold, based on the asymmetry described above. We utilize three different models for reconstructing fault slip: 1) a fault-propagation fold with kink-band geometry [*Suppe and Medwedeff*, 1990] above a shallow, subhorizontal décollement, 2) a hybrid fault-propagation/detachment fold developed above a planar ramp [*Chester and Chester*, 1990; *Marrett and Bentham*, 1997], and 3) as a trishear fault propagation fold [*Erslev*, 1991; *Hardy and Ford*, 1997]. All models share an assumption that deformation occurs by plane strain, so that area is conserved and the excess vertical area (in the deformed state) above the original, undeformed elevation of the unconformity is equal to the area transferred into the section along the basal fault [*Mitra and Namson*, 1989]. The first two models involve the assumption that line-length of the unconformity is conserved. Finally, in the trishear model, unconformity line-length is not conserved, and the total shortening across the section equals the horizontal component of slip along the fault.

The shallow décollement model accounts for transfer of material into the section by unconformity-parallel shear. Estimation of the amount of shear involves construction of a shortening profile using selected unconformity-parallel horizons (with the assumption of line-length conservation) at various depths in the basement. To calculate the depth to detachment, we take the excess area above the unconformity and subtract the amount of area transferred into the section by unconformity-parallel shear from the hinterland. Depth to detachment equals the corrected excess area divided by the total shortening of the unconformity [*Mitra and Namson*, 1989].

In the shallow décollement model, we model the southwestern anticline as a fault-bend fold with a flat crest (Figure 7a). Restoration of the anticlines (Figure 7b) yields a relatively limited estimate of total shortening across the section: 1.4 km (~7% of the exposed cross-section). This reflects the minimum amount of shortening that can elevate the unconformity in the crest of the frontal fault-propagation fold above the present-day land surface, exposing Permian bedrock in the core. An alternative interpretation of the maximum allowable shortening is constrained by the blind fault tip. If we allow the fault tip to have propagated just enough to reach the present-day land surface, we arrive at an estimate of 2.1 km (~11% of the exposed cross-section). In either estimate, most of the shortening is accomplished on the frontal fold; the southern structures are relatively minor. Moreover, this model shown does not adequately explain the inferred northeastward-dipping panel (Figure 7a) and the exposure of Carboniferous basement at the southwestern end of the cross-section (Figure 4). An additional structure to the southwest may be required in order to explain the inferred deformation at the southwestern end of the cross-section. We expect, from the relatively shallow dips in nearby exposures of Neogene sediments (Figure 4), however, that such a structure would be relatively minor.

Recognizing that the subhorizontal décollement model is likely not applicable to faults propagating through steeply dipping bedrock, we also model the frontal anticline as a hybrid fault-propagation/detachment fold [*Chester and Chester*, 1990; *Marrett and Bentham*, 1997]. This interpretation considers the frontal anticline as a fold formed above a fault plane of constant dip that extends deeper into the crust. In the absence of evidence for or against changes in bed thickness, models presented here assume constant bed thickness, such that unconformity-parallel line-length is conserved. The presence of the unconformity in the hanging wall places a limit on the amount of fault propagation and slip that can occur before the unconformity is elevated above the present-day land surface (Figure 7c, d). Restoration adhering to this constraint yields a minimum amount of shortening of ~0.8 km shortening (Figure 7d). The structure can accommodate additional shortening if the interpreted depth of the unconformity prior to deformation is somewhat greater. This allows up to ~1.1 km of shortening. Note that our interpretations do not include a bend in the fault at depth (into a horizontal detachment) because of the lack of observed field evidence for a fault bend fold south of the range front.

In the trishear model, a fold forms as beds are deformed within a triangular shear zone in front of the propagating fault tip. The trishear model was developed to explain deformation above Laramide-type fault-propagation folds in settings where faulting involves both basement rocks and overlying sedimentary cover [*Erslev*, 1991; *Erslev and Rogers*, 1993]. We used the program FaultFold (created by Rick Allmendinger) to model the frontal fold as a trishear fault-propagation fold. Trishear models with a horizontal décollement yield a minimum shortening estimate of 2.4 km (or 20% of the exposed cross-section; Figure 7e,f) and a maximum estimate of 3.0 km (or 24% of the exposed cross-section; Figure 7g,h). Models with a dipping detachment require a change in the dip of the fault at depth in order to reproduce the inferred backlimb fold geometry (Figure 7i). These models yield minimum and maximum shortening estimates of 1.5 km (or 11% of the exposed cross-section; Figure 7j) and 1.9 km (or 15% of the exposed cross-section) respectively.

All three models are in general agreement with the observed fold and fault geometry, highlighting the uncertainty of reconstructing fault geometry from surface measurements alone.

Modeled fault dips range from 34° SW in the shallow décollement model to 47° SW in the trishear model with a dipping detachment, consistent with the range of fault dips estimated along the frontal part of the range (Table 1). Moreover, projection of the unconformity from its elevation where it crosses the nose of the fold (Figure 4), along the inferred fold axis, and into the plane of the cross-section yields a predicted elevation of ~3100 m for the unconformity in the fold crest. For each class of models, the amount of shortening necessary to elevate the unconformity to 3100 m lies within the range of estimated shortening. Although all three classes of models yield estimates of shortening between 1-3 km, we tend to favor estimates derived from the trishear model, simply because it is likely most applicable to the setting of sedimentary rocks overlying a basement-involved thrust system where the ‘basement’ rocks are themselves steeply dipping. The shallow décollement model predicts transfer of material by shear parallel to Neogene layers; such shearing would likely be inhibited if bedrock layering was oblique to Neogene strata (Figure 4). Regardless of the choice of model, however, the geometry of folding along the Tao river indicates that the West Qinling fault system accomplished relatively minor shortening during Tertiary time.

4.2. Constraints on shortening within the Tibetan Plateau from the Meiwu surface

One of the challenges to reconstructing the magnitude of Cenozoic shortening throughout the Tibetan Plateau is deconvolving earlier deformational events. In the region south of the Linxia basin, Paleozoic and Triassic units in the high plateau exhibit significant deformation in the form of km-scale upright, isoclinal folds and laterally-extensive reverse faults (Figures 3 and 8). Few direct constraints on fault plane orientations are available; however, deformed units dip steeply throughout the region (Figure 8), and it is self-evident that these geometries require significant shortening of Paleozoic and Mesozoic strata.

As described above, however, the topographic surface of the plateau throughout much of this region exhibits extremely low topographic relief (Meiwu surface). Similar surfaces in eastern and southeastern Tibet appear to pre-date Cenozoic development of high topography [*Clark, et al.*, 2006], and it is likely that the Meiwu surface represents a relict landscape, partially buried beneath Neogene rocks. Regardless of its absolute age, however, the geometry of the surface cross-cuts steeply dipping Permian and Carboniferous units. This relationship, coupled with the presence of thrust faults that displace Mesozoic and Paleozoic units but are themselves overlapped by Neogene sediments (Figure 3), indicates that much of the deformation recorded in the Paleozoic bedrock developed prior to Cenozoic time. Thus, preservation of the undeformed surface atop the plateau suggests that this region has experienced little internal deformation during Tertiary time. Rather, shortening related to plateau development appears to be concentrated at the north and south flanks of the Meiwu surface, adjacent to the Linxia and Lintan basins, respectively.

4.3. Shortening estimates at the margin of the Lintan Basin

To place bounds on the amount of shortening across the margin of the Lintan basin, we take a similar approach to reconstructing balanced cross-sections (Figure 9). At the northern margin of the Lintan basin, an ESE-striking, southwest-vergent reverse fault places Eocene and Triassic bedrock in the hanging wall over Neogene sediments in the footwall (Figure 3). Unfortunately, only a few remnant exposures of Neogene deposits are present north of the thrust fault (Figure 3), providing limited constraints on the magnitude of shortening. An exposure of Neogene sediment in the hanging wall dips gently north, while sediments in the footwall adjacent to the fault dip steeply south, suggesting that the structure formed as a SW-vergent fault-propagation fold. Given the similarity between results of the trishear and other models on the Linxia basin margin, we present only the results of a trishear model for this structure. Trishear models of the structure as a fault-propagation fold with a horizontal décollement yield minimum and maximum shortening estimates of 2.4 km (~11%; Figure 9ea,b) and 6.5 km (~31%; Figure 9c,d), respectively. For trishear models with a dipping detachment, only one interpretation of the degree of fold development is admissible (Figure 9e); this interpretation yields a shortening estimate of 1.0 km (or 5% of the exposed cross-section; Figure 9f).

Mapped relations (Figure 4) indicate that the fault tip breaks the surface at the contact between Neogene sediments and older bedrock at the northern edge of the Lintan basin. In order for models presented here to be admissible, the fault tip must subsequently propagate upward at a steep angle to cut the forelimb of the fold in a high-angle breakthrough [*Suppe and Medwedeff*, 1990]. Measurements farther west along the fault system [*Ministry of Geology and Mineral Resources*, 1989] suggest a fault plane dip of approximately 60º where the fault breaks the surface (Figure 9). In the absence of precise cutoffs, the amount of slip along the fault that could have occurred after such a breakthrough is unclear. Thus, our estimates all provide only minimum bounds on the magnitude of shortening. We suggest, however, that this preliminary estimate is also consistent with relatively limited shortening observed along the West Qinling fault system.

5. LOW TEMPERATURE THERMOCHRONOLOGY

Although structural analysis provides insight into the mechanisms and magnitude of Tertiary deformation in this region, the timing and rates of shortening remain uncertain. The cooling histories of rocks exposed in the hanging wall of major thrust systems can place bounds on the exhumational history of the range, and by inference, the timing of topographic relief development in response to fault activity [e.g., *Bullen, et al.*, 2003; *Bullen, et al.*, 2001]. In order to refine our understanding of the onset of exhumation in the hanging-wall of the West Qinling fault system, we collected a suite of ten bedrock samples, spanning ~900m in elevation, from an exposed granodioritic pluton, located approximately midway between the Tao He and Daxia He (Figure 4) for (U-Th)/He apatite thermochronometry. The (U-Th)/He thermochronologic system has a relatively low closure temperature in apatite [~65°C, *Farley*, 2000; *Wolf, et al.*, 1996] which makes it a useful tool for determining thermal histories in the shallow crust [e.g., *Lippolt, et al.*, 1994; *Wolf, et al.*, 1998; *Wolf, et al.*, 1996; *Zeitler, et al.*, 1987].

Apatites were concentrated from hand samples using mechanical and density separation methods (R. Donelick, pers. communication). Individual apatite grains were hand picked for (U-Th)/He analysis at the California Institute of Technology. Equant grains devoid of visible inclusions were selected, and the dimensions of each grain were measured. Grains ranged from 80 μm to 170 μm in prism half-width and F_t values [*Farley, et al.*, 1996] ranged from 0.67 to 0.83 (Table 2). For each analysis, a single grain was loaded into a platinum packet, and laser heated in a vacuum to 1050˚C for five minutes to release all helium. Helium was measured in a quadrupole mass spectrometer using ^{3}He isotope dilution [for a description of the apparatus, seem *Wolf, et al.*, 1996]. Samples were re-heated to ensure complete release of helium; samples that yielded significant re-extraction of gas were presumed to host micro-inclusions of a more retentive phase, and are excluded from sample means (Table 1). After gas extraction, each grain was placed in HNO_3, spiked with ^{235}U and ^{230}Th, and heated to 60˚C for one hour to facilitate complete dissolution. The solution was analyzed on an inductively coupled plasma mass spectrometer (ICP-MS) for uranium and thorium content. Raw ages were calculated for each replicate, and an alpha-ejection correction was applied based on the measured size of the grain

[*Farley, et al.*, 1996]. Mean ages were calculated from between 3 - 8 individual grains from each sample (Table 2).

Mean corrected ages for the apatites span a time period of ~35 m.y. and exhibit a linear correlation between mean age and elevation (Figure 10). We observe, however, that some samples exhibit a wide range of ages among individual replicate analyses. In particular, samples 04-09, collected near the base of the transect, and 04-04, collected near the top of the transect, exhibit considerable age variability in replicated ages (Table 2). These apatites also display a strong correlation between helium content and age (Table 2) that may reflect either anomalous helium loss (due to weathering or transient thermal effects associated with range fires) or from implantation of helium within apatite grains (due to adjacent radiogenic mineral phases). An additional sample (05-05) was collected during 2005 from the same outcrop as 04-09; although the scatter in replicate ages is reduced (Figure 10), a correlation with He concentration remains (Table 2). Regardless of the cause of the correlation, we consider the mean ages from these samples unreliable, and we do not include them in our interpretation (Figure 10).

A second sample at the base of the transect (04-10) lies below the projection of the age-elevation trend (Figure 10). However, this sample was collected several kilometers downstream of the primary age-elevation transect, near the West Qinling fault, and it's older age may reflect topographic effects during cooling [*Stüwe, et al.*, 1994] and/or localized thermal effects near the fault. Moreover, this sample exhibits a correlation between age and the grain-size correction (Ft), consistent with observations of samples that have experienced slow cooling [*Reiners and Farley*, 2001]. Because of the wide range of replicate ages, we consider this mean age to be unreliable and we restrict our interpretation of the cooling history to the upper ~700 m of the transect (Figure 10).

A significant feature of these (U-Th)/He age data is the low slope of the age-elevation relationship, suggestive of slow cooling over the period from ~55 to ~20 Ma (Figure 10a). For a sampling transect in which the samples vary both in vertical position and horizontal position, direct inference of an exhumation rate from the slope of the age-elevation relationship requires the assumption that the closure isotherm remained fixed in space and time (Ehlers, 2005). Generally, this assumption is only valid under slow exhumation rates, such that advection of heat is negligible [*Braun*, 2005; *Ehlers*, 2005; *Mancktelow and Grasemann*, 1997; *Stüwe, et al.*, 1994].

In our study, the Meiwu surface places an additional constraint on the interpretation of low-temperature thermochonologic data. If the Meiwu surface represents a continuous, low-relief landscape that pre-dates the cooling and exhumation of the samples, the surface may provide a more appropriate datum from which to reference the paleo-depth of samples. Similar low-relief surfaces have been utilized in this way to interpret apatite (U-Th)/He ages in the Sierra Nevada [*Clark, et al.*, 2005b], in southeastern Tibet [*Clark, et al.*, 2005a], and near our study area in northeastern Tibet, along the Daxia River [*Clark, et al.*, 2004].

Projection of the Meiwu surface northward over the location of the sampling transect permits use of the projected elevation as a datum for referencing the vertical positions of individual samples (Figure 10b). The surface climbs slightly in elevation toward its northern edge along the crest of the West Qinling, imparting a degree of uncertainty into the projection of this surface above the present-day range front. In addition, whether the surface is folded above the West Qinling fault in this region is unknown. Because of these possibilities, we assign greater depth uncertainties (Figure 10b) than those in the age-elevation relationship.

Regardless of reference frame (Figure 10), both the age-elevation and age-depth relationships suggest similar denudation rates in the upper part of the transect; the age-elevation regression yields a slope of ~17 m/Myr (Figure 10a) and the age-depth regression yields a slope of ~13 m/Myr (Figure 10b). The similarity in estimated rates provides confidence in the interpretation that denudation rates in this part of the West Qinling were slow from ~55 Ma to ~20 Ma. This result is consistent with thermal histories derived from age-elevation relationships in southeastern Tibet [*Clark, et al.*, 2005a] and adjacent to the Sichuan Basin [*Kirby, et al.*, 2002]. Both of these studies document a protracted period of slow cooling that followed Mesozoic deformation in the Songpan-Garze terrane and appears to have continued up into Miocene time [*Kirby, et al.*, 2002]. It is noteworthy that all of these studies documenting slow cooling during the late Mesozoic and early Cenozoic in northeastern Tibet were conducted near preserved remnants of low-relief surfaces, and it appears likely that these landscapes may have once been correlative [e.g., *Clark, et al.*, 2006].

In addition to the regional implications, the combination of low denudation rates implied by our data and the presence of the Meiwu surface place some bounds on the timing of deformation along the West Qinling fault system in this part of northeastern Tibet. Shortening associated with slip along the West Qinling fault system is likely to have been associated with the generation of significant topographic relief, at least during local fold growth. There is no indication of rapid cooling in our data set, suggesting that any increase in cooling rate associated with thrust activity must postdate the youngest age from our transect. Thus, our data imply that the development of the present-day relief in the West Qinling, and by inference, shortening along the West Qinling fault system, occurred at some time more recently than ca. 20 Ma. In principle, one could make a coarse estimate of the depth at which this rapid cooling would be recorded.

Assuming a geotherm of ~20°C/km, the closure isotherm for helium in apatite should reside at ~3 km below the relict surface, or ~ 1km below the present-day land surface.

It is intriguing that our data suggest slow cooling during Eocene - Oligocene time, a period that spans the onset of sediment accumulation in the Linxia Basin [*Fang, et al.*, 2003]. It is possible that the source area for this sediment was farther to the south or west at this time, but this speculation remains untested. Ongoing work on an adjacent (U-Th)/He elevation transect farther west (in the canyon of the Daxia River, Figure 1) appears to preserve evidence for a short-lived episode of increased denudation rate at ca. 45 Ma [*Clark, et al.*, 2004]. However, the episode appears to be followed again by relatively slow denudation (ca. 50 m/m.y.) extending to ca. 10 Ma [*Clark, et al.*, 2004]. Thus, although a more precise characterization of late Eocene-early Oligocene cooling south of the Linxia basin awaits additional sampling and analysis, both data sets suggest that development of much of the relief along the southern margin of the Linxia basin occurred sometime more recently than 18 - 10 Ma. We infer that the majority of slip on the West Qinling fault and deformation associated with the leading-edge fold in the Tao River region is Late Miocene or younger.

6. IMPLICATIONS FOR PLATEAU GROWTH IN NORTHEASTERN TIBET

Our analysis of deformation at the northeastern margin of the Tibetan Plateau indicates that Tertiary shortening adjacent to the Linxia Basin was limited to 1-3 km. Moreover, preservation of the Meiwu surface atop the plateau indicates that this region of northeastern Tibet experienced little internal deformation during Tertiary time; shortening was instead concentrated at the northern and southern flanks of the range, adjacent to the Linxia and Lintan basins, respectively. Combination of shortening across these two fault systems thus yields a total estimate of shortening across a large, contiguous portion of the plateau (Figure 1). In the discussion, we consider the results of modeling folds with trishear kinematics, as these probably represent the most likely representation of the actual fold mechanics. For these models, total shortening between the Lintan and Linxia basins ranges from ~3 – 10 km (Table 3). We note that these are among the highest estimates; other models of fault geometry yield lower values (Table 3).

We might expect shortening to be somewhat larger near the center of the West Qinling fault, as most fault systems exhibit a systematic scaling of displacement with fault length [*Cowie and Scholz*, 1992; *Schlische, et al.*, 1996]. Established scaling relationships for thrust faults [*Davis, et al.*, 2005; *Schlische, et al.*, 1996] can provide an approximate bound on the amount of deformation possible near the center of the fault (roughly located near the Daxia river, Figure 1). Global scaling relationships suggest that maximum fault displacement for the ~90 km segment of the West Qinling fault that bounds the Linxia Basin should be on the order of 3-4 km. There is some ambiguity in fault length (75 – 110 km), depending on whether the segment is linked with a mapped fault segment to the west (Figure 1). These ambiguities suggest that maximum fault displacement could be as high as ~5-6 km. Although inferences from displacement-length scaling represent only crude estimates of fault displacement, the correspondence between these estimates and our maximum estimates from cross-section reconstruction corroborates our inference that Tertiary shortening is limited (<10 km) across this fault system. The West Qinling thrust is in many ways similar to Laramide-style fault-fold systems that accomplish relatively limited shortening of the upper crust [e.g., *Erslev and Rogers*, 1993].

We turn to the question of whether the observed shortening is sufficient to generate present-day crustal thickness in northeastern Tibet. Simple calculations assuming local (Airy) isostatic compensation of the high mean elevations south of the Linxia Basin (~3200 – 3400 m) yield estimates of crustal thickness of approximately 56-58 km (choosing a sea-level reference column of thickness 35 km and ρ_c = 2800 kg/m^3, and ρ_m = 3300 kg/m^3). This value is in general agreement with other estimates at the northeastern plateau margin based on regional seismic tomography [55-57 km, *Li and Mooney*, 1998; *Li, et al.*, 2002] and on S-wave receiver functions [~57-km, *Chen, et al.*, 2004]. Our measures of upper crustal shortening permit an evaluation of the contribution of this process to the present-day thickness, based on the assumption of plane strain (conservation of area) and the conservative assumption that upper crustal shortening estimates are representative of the entire crustal column. Assuming an initial crustal thickness of 35 km, our minimum (2.9 km) and maximum (9.9 km) shortening estimates predict final thicknesses of 37 km and 42 km, respectively. These estimates fall short of the inferred present-day crustal thickness of 55-60 km beneath the northeastern plateau, implying that either: 1.) the crust in this region was already significantly thickened prior to the Tertiary, or 2.) there was an additional source of crustal thickening during the growth of the plateau.

Our simple analysis implies that the crust would have had to be ~50-55 km thick, prior to Tertiary shortening, in order to generate the present-day crustal structure. We can, to some degree, evaluate this possibility by considering the along-strike continuation of the Qinling orogen, east of our study area (Figure 1). The Qinling represent the remnant of a late Paleozoic-early Mesozoic mountain belt formed during the collision between the North and South China cratons [*Mattauer, et al.*, 1985]. The eastern portion of this orogen, north of the Sichuan Basin, appears to be east of the region of thickened crust of the northeastern Tibetan Plateau (although this view has been recently challenged[*Enkelmann, et al.*, 2006]); thus, it may provide a reasonable estimate of the pre-collision crustal thickness in the western Qinling. Again assuming

Airy isostasy, mean elevations of ~1200-1500 m in the Qinling Shan imply crustal thicknesses between 43-45 km for the eastern Qinling Shan, in general agreement with global seismic estimates [40-45 km, *Li and Mooney*, 1998].

Although this analysis is clearly simplified, in that it does not account for flexural support of topography and/or variations in initial crustal thickness along the Qinling, it suggests that, to first-order, shortening of the upper crust in northeastern Tibet is not sufficient to accomplish present-day crustal thicknesses and elevations. Thus, our results support models for the growth of eastern Tibet that invoke thickening and flow in the lower crust [e.g., *Clark and Royden*, 2000]. We note that this process has recently been invoked to explain young cooling ages in the Qinling, east of our study area [*Enkelmann, et al.*, 2006]. If the central Qinling has experienced recent thickening of the lower crust, this would imply that our estimates of pre-collisional thickness are too large, requiring a greater source of crustal material. In general, the northeastern corner of the plateau may hold the key to deconvolving the contributions of shortening at different crustal levels to the growth of high topography in Asia. Our study highlights the need to more completely understand the distribution of crustal thickness and topography prior to the Indo-Asian collision in addition to the distribution of Tertiary shortening in space and time.

7. CONCLUSIONS

Our mapping in the Tao He region of the West Qinling range, reconstruction of deformation across the West Qinling fault system, and thermochonology from the hanging-wall rock lead us to the following conclusions:

1.) Tertiary shortening in the northeastern corner of the Tibetan Plateau is localized on the margins of the Linxia and Lintan basins. North- and south-vergent fault systems that bound the margins of these basins, respectively, are moderate to steeply dipping reverse faults. Associated folding in Neogene sediments suggests that these structures grew as fault-propagation folds with geometries reminiscent of Laramide-type structures that involve basement deformation.

2.) Restoration of balanced cross-sections across the West Qinling thrust fault yields estimates of Tertiary upper crustal shortening on structures at the southern margin of the Linxia basin that range from 1 - 3 km. A reconnaissance analysis of the fault system along the northern edge of the Lintan basin yields poorly-resolved shortening between 1 – 6.5 km.

3.) The low-relief landscape of the Meiwu plateau appears to correlate to the basal depositional contact of Neogene sediments adjacent to the Linxia Basin. Moreover, this surface was developed across steeply deformed Paleozoic bedrock in the plateau south of the basin, indicating that much of the deformation in the middle of the range predates the Tertiary. Thus, we are able to develop a regional budget of Tertiary deformation that is limited to the fault systems adjacent to the Linxia and Lintan basins.

4.) (U-Th)/He ages in apatite from the southern margin of the Linxia basin exhibit a correlation with elevation that is consistent with slow cooling from ~55 Ma to ~20 Ma. This relationship suggests the presence of a partial retention zone for helium in apatite below the Meiwu surface. Inferred denudation rates of 15-20 m/Myr are consistent with slow erosion atop this landscape since at least Paleocene time. We infer that the development of the present-day high relief on the range front, and associated slip on the West Qinling fault system, occurred at some time younger than ~ 20 Ma. Thus, our results are consistent with a pulse of Miocene tectonism throughout northeastern Tibet.

5.) Overall, our results suggest that upper crustal shortening in northeastern Tibet is not sufficiently large to account for the present-day crustal thickness. We suggest, therefore, that our results imply an additional source of crustal thickening, perhaps associated with flow of lower crust from beneath the central plateau.

ACKNOWLEDGEMENTS

This research was supported by a grant from the NSF Continental Dynamics program (EAR-0506622). CA acknowledges support from a university graduate fellowship at Penn State and the Krynine fund. Paleocurrent measurements were plotted using GeoPlot, created by Steve Ahlgren, and trishear modeling was accomplished using FaultFold created by Rick Allmendinger. We thank Yuan Daoyang and Wang Zhicai for discussions in the field and Lindsey Hedges for assistance at Caltech.

FIGURE CAPTIONS

Figure 1. Tectonic setting of Tertiary basins and faults in the northeastern Tibetan Plateau. Background is a color-shaded relief map generated from Shuttle Radar Topography Mission (SRTM) data (NASA, 2003; source for the dataset is http://srtm.csi.cgiar.org/). Tertiary basins are shown in yellow. The Yellow River and major tributaries (Daxia and Tao rivers) are labeled in blue. Box (dashed line) shows location of study area. Inset: shaded relief map of the Indo-Asian collision zone. White box shows location of Figure 1. Abbreviations are as follows: GH - Gong He Basin, G – Guide Basin, LJ - La Jie Shan, LX - Longxi Basin, XH – Xun Hua Basin.

Figure 2. Topography of the northeastern Tibetan Plateau. **A.** 90 meter digital elevation model (DEM) from the NASA Shuttle Radar Topography Mission (SRTM) data. Elevation values are in meters. D = Daxia River, T = Tao River. Dashed box shows outline of map in Figure 4. **B.** Land surface slope at each cell in the DEM in degrees. Note high slopes near major rivers on the plateau. **C.** Filtered results highlighting areas of low slope (< 10°) and low curvature (Laplacian of topographic surface, $\nabla^2 z$). **D.** Map of Tertiary-Quaternary sediments [*Ministry of Geology and Mineral Resources*, 1989; 1991]. Note that most of the low relief surfaces shown in C are Tertiary-Quaternary basins. Basin symbols: LX = Linxia, L = Lintan, G = Ganjia, T = Tongren, H = Hezuo, S = Sangke.

Figure 3. Geologic map showing distribution and structure of Mesozoic and Paleozoic bedrock south of the Linxia basin. Geology is based on 1:200,000 geologic maps [*Ministry of Geology and Mineral Resources*, 1989] and on our own mapping. Extent of Meiwu low-relief surface is shown as shaded region. Faults that do not truncate Neogene units are shown in gray. Faults that demonstrably displace Neogene deposits are shown in black. Blue lines show locations of cross-sections.

Figure 4. Enlarged geologic map of Neogene deposits in the vicinity of the Tao river. Bedding orientations (black) and fold axes within the Neogene units are from our mapping. Also shown are the locations of thermochronologic samples (blue circles). Units and symbols follow the legend in Figure 3. Inset stereonet shows poles to strike and dip measurements from forelimb (squares) and backlimb (circles) of frontal fold. Great circle shows best-fit plane to measurements; pole to this plane (shown as X) represents the macroscopic fold axis. Dashed box shows area of Figure 6.

Figure 5. Geometry of folding at the West Qinling range front. **A.** View of the ESE plunging frontal anticline, looking NE from within the plateau. Dashed line highlights unconformity where Neogene sediments extend across the fold (see Figure 4). Black lines show fold axes. **B.** Cross-section (see Figure 4 for trace) through Neogene sediments west of the Tao River, showing inferred geometry of the frontal anticline. Photos show gently south to southeast dipping backlimb and steeply northeast dipping forelimb, with bedding highlighted. **C.** Cross-section (see Figure 4 for trace) through Cretaceous rocks E of the Tao River, showing steep dips near the range front and decreasing dips to the N. Photo shows northward dipping Cretaceous rocks at the range front.

Figure 6. Map showing paleocurrent data from Neogene sediments. All pre-Neogene rocks are shown in white for clarity; fold axes are shown in grey and thrust faults in black. Rose diagrams show measured down-current flow direction at each site based on measurement of imbricated clasts (rotated to correct for bedding dip); line indicates mean down-current direction. Rose diagrams generated using GeoPlot software (created by Steve Ahlgren). Site numbers in bold; n = number of measurements at each site. Location of this area is shown as dashed box in Figure 4.

Figure 7. Models of anticlines at the range front adjacent to the Linxia basin. **A.** Model of frontal anticline as a fault-propagation fold and rear anticline as a fault-bend fold, interpreted to yield a minimum shortening estimate. **B.** Restored. **C.** Model of frontal anticline as a hybrid fault-propagation/detachment fold, interpreted to yield a minimum shortening estimate. **D.** Restored. **E.** Model of frontal anticline as a trishear fault-propagation fold with a horizontal detachment, interpreted to yield a minimum shortening estimate. **F.** Restored. **G.** Trishear fold model with horizontal detachment yielding a maximum shortening estimate. **H.** Restored. **I.** Trishear fold model with dipping detachment yielding a minimum shortening estimate. **J.** Restored. Images in E-J are based on graphics output from the program FaultFold, created by Rick Allmendinger. Beds in E-J highlighted to show forelimb thickening. No vertical exaggeration in A-J.

Figure 8. Schematic cross-section through Mesozoic and Paleozoic bedrock of the West Qinling range. Fault locations, unit ages and distributions, and strike and dip measurements are from [*Ministry of Geology and Mineral Resources*, 1989]. Topographic profile derived from SRTM data. Note that the low relief surface of the Meiwu plateau cross-cuts steeply dipping Paleozoic bedrock.

Figure 9. Reconnaissance-level models of Tertiary structure at the northern margin of the Lintan basin. Thick gray lines show possible paths for high-angle breakthrough of the fault tip. **A.** Model of frontal anticline as a trishear fault-propagation fold with a horizontal detachment, interpreted to yield a minimum shortening estimate. **B.** Restored. **C.** Trishear fold model with horizontal detachment yielding a maximum shortening estimate. **D.** Restored. **E.** Trishear fold model with dipping detachment. **F.** Restored. Vertical exaggeration in A-D equals 0.5x. No vertical exaggeration. Images are based on graphics output from the program FaultFold, created by Rick Allmendinger. Beds highlighted to show deformation in forelimb.

Figure 10. (U-Th)/He ages for apatite samples from a granite pluton in the hanging wall of the West Qinling fault. Sample locations are shown in Figure 4. Regressions exclude only samples exhibiting correlations between He concentration and age (open circles). **A.** Plot of mean corrected (U-Th)/He ages and sample elevations. Error bars show the range of replicate ages for each sample. **B.** Mean corrected (U-Th)/He ages and sample depths below the projected low-relief Meiwu surface. Horizontal error bars show the range of replicate ages. Vertical error bars reflect uncertainty in the projection of the relict surface.

REFERENCES CITED

Argand, E. (1924), La tectonique de l'Asia, paper presented at Proceedings 13th Int. Geol. Congress, Brussels.

Beaumont, C., et al. (2001), Himalayan tectonics explained by extrusion of a low-viscosity crustal channel coupled to focused surface denudation, *Nature*, *414*, 738-742.

Braun, J. (2005), Quantitative constraints on the rate of landform evolution derived from low-temperature thermochronology, in *Low-temperature thermochronology: techniques, interpretations, and applications*, edited by P. W. Reiners and T. A. Ehlers, pp. 351-374, Mineralogic Society of America.

Bruguier, O., et al. (1997), U-Pb dating on single detrital zircon grains from the Triassic Songpan-Ganzi flysch (central China): Provenance and tectonic correlations, *Earth and Planetary Science Letters*, *152*, 217-231.

Bullen, M. E., et al. (2003), Building the northern Tien Shan: Integrated thermal, structural, and topographic constraints, *The Journal of Geology*, *111*, 149-165.

Bullen, M. E., et al. (2001), Late Cenozoic tectonic evolution of the northwestern Tien Shan: New age estimates for the initiation of mountain building, *Geological Society of America Bulletin*, *113*, 1544-1559.

Burchfiel, B. C., et al. (1995), Tectonics of the Longmen Shan and adjacent regions, *International Geology Review*, *37*, 661-735.

Burchfiel, B. C., et al. (1989), Intracrustal detachments within zones of intracontinental deformation, *Geology*, *17*, 478-452.

Chang, E. Z. (2000), Geology and tectonics of the Songpan-Ganzi fold belt, southwestern China, *International Geology Review*, *42*, 813-831.

Chen, J. H., et al. (2004), Crust and upper mantle S-wave velocity structure across northeastern Tibetan Plateau and Ordos Block, *Chinese Journal of Geophysics*, *47*, 1-15.

Chester, J. S., and F. M. Chester (1990), Fault-propagation folds above thrusts with constant dip, *Journal of Structural Geology*, *12*, 903-910.

Clark, M. K., et al. (2004), Exhumation and plateau growth in northeastern Tibet, *EOS Trans. AGU*, *85(47)*, Fall Meeting Supp., Abstract T33D-08.

Clark, M. K., et al. (2005a), Late Cenozoic uplift of southeastern Tibet, *Geology*, *33*, 525-529.

Clark, M. K., et al. (2005b), The non-equilibrium landscape of the southern Sierra Nevada, California, *GSA TOday*, *15*, 4-10.

Clark, M. K., and L. H. Royden (2000), Topographic ooze: Building the eastern margin of Tibet by lower crustal flow, *Geology*, *28*, 703-706.

Clark, M. K., et al. (2006), Use of a regional, relict landscape to measure vertical deformation of the eastern Tibetan Plateau, *Journal of Geophysical Research*, *111*, doi:10.1029/2005JF000294.

Cowie, P. A., and C. H. Scholz (1992), Displacement-length scaling relationship for faults: data synthesis and discussion, *Journal of Structural Geology*, *14*, 1149-1156.

Currie, B. S., et al. (2005), Middle Miocene paleoaltimetry of southern Tibet: Implications for the role of mantle thickening and delamination in the Himalayan orogen, *Geology*, *33*, 181-184.

Davis, K. D., et al. (2005), Thrust-fault growth and segment linkage in the active Ostler fault zone, New Zealand, *Journal of Structural Geology*, *27*, 1528-1546.

Deng, T., et al. (2004), Sequence of Cenozoic mammalian faunas of the Linxia basin in Gansu, China, *Acta Geologica Sinica*, *78*, 8-14.

Dettman, D. L., et al. (2003), Uplift-driven climate change at 12 Ma: a long $\delta^{18}O$ record from the NE margin of the Tibetan plateau, *Earth and Planetary Science Letters*, *6764*, 1-11.

Dupont-Nivet, G., et al. (2004), Paleogene clockwise tectonic rotation of the Xining-Lanzhou region, northeastern Tibetan Plateau, *Journal of Geophysical Research*, *109*.

Ehlers, T. A. (2005), Crustal thermal processes and the interpretation of thermochronometer data, in *Low-temperature thermochronology: techniques, interpretations, and applications*, edited by P. W. Reiners and T. A. Ehlers, pp. 315-350, Mineralogic Society of America.

England, P., and G. Houseman (1986), Finite strain calculations of continental deformation 2. Comparison with the India-Asia collision zone, *Journal of Geophysical Research*, *91*, 3664-3676.

Enkelmann, E., et al. (2006), Cenozoic exhumation and deformation of northeastern Tibet and the Qinling: Is Tibetan lower crustal flow diverging around the Sichuan Basin?, *Geological Society of America Bulletin*, *118*, 651-671.

Erslev, E. A. (1991), Trishear fault-propagation folding, *Geology*, *19*, 617-620.

Erslev, E. A., and J. L. Rogers (1993), Basement-cover geometry of Laramide fault-propagation folds, in *Laramide basement deformation in the Rocky Mountain foreland of the Western United States*, edited by C. J. Schmidt, et al., pp. 125-146, Special Paper - Geological Society of America.

Fang, X., et al. (2003), Flexural substance by 29 Ma on the NE edge of Tibet from the magnetostratigraphy of Linxia Basin, China, *Earth and Planetary Science Letters*, *210*, 545-560.

Fang, X., et al. (2005), Late Cenozoic deformation and uplift of the NE Tibetan Plateau: Evidence from high-resolution magnetostratigraphy of the Guide basin, Qinghai Province, China, *Geological Society of America Bulletin*, *117*, 1208-1255.

Farley, K. A. (2000), Helium diffusion from apatite: General behavior as illustrated by Durango fluorapatite, *Journal of Geophysical Research*, *105*, 2903-2914.

Farley, K. A., et al. (1996), The effects of long alpha-stopping distances on (U-Th)/He ages, *Geochimica et Cosmochimica Acta*, *60*, 4223-4229.

Garzione, C. N., et al. (2005), Source of Oligocene to Pliocene sedimentary rocks in the Linxia basin in northeastern Tibet from Nd isotopes: Implications for tectonic forcing of climate, *Geological Society of America Bulletin*, *117*, 1156-1166.

Garzione, C. N., et al. (2006), Rapid late Miocene rise of the Bolivian Altiplano: Evidence for removal of mantle lithosphere, *Earth and Planetary Science Letters*, *241*, 543-556.

Hao, Y. C. (1988), Cretaceous and Palaeogene ostracod biostratigraphy in Xining and Minhe basins of China, in *Evolutionary Biology of Ostracoda*, edited by T. Hanai, et al., pp. 1163-1171, Elsevier Scientific, New York.

Hardy, S., and M. Ford (1997), Numerical modeling of trishear fault propagation folding, *Tectonics*, *16*, 841-854.

Horton, B. K., et al. (2004), Mesozoic-Cenozoic evolution of the Xining-Minhe and Dangchang basins, northeastern Tibetan Plateau: Magnetostratigraphic and biostratigraphic results, *Journal of Geophysical Research*, *109*, B04402.

Horton, B. K., et al. (2002), Paleocene-Eocene syncontractional sedimentation in narrow, lacustrine-dominated basins of east-central Tibet, *Geological Society of America Bulletin*, *114*, 771-786.

Kapp, P., et al. (2003a), Mesozoic and Cenozoic tectonic evolution of the Shiquanhe area of western Tibet, *Tectonics*, *22*, 1029 (1023:1021-1023:1024).

Kapp, P., et al. (2005), Cretaceous-Tertiary shortening, basin development, and volcanism in central Tibet, *Geological Society of America Bulletin*, *117*, 865-878.

Kapp, P., et al. (2003b), Tectonic evolution of the early Mesozoic blueschist-bearing Qiangtang metamorphic belt, central Tibet, *Tectonics*, *22*, 1043 (1017:1041-1017:1025).

King, R. W., et al. (1997), Geodetic measurement of crustal motion in southwest China, *Geology*, *25*, 179-182.

Kirby, E., et al. (2002), Late Cenozoic uplift and landscape evolution along the eastern margin of the Tibetan Plateau: Inferences from 40Ar/39Ar and (U-Th)/He thermochronology, *Tectonics*, *21*, 1-1 - 1-20.

Kirby, E., et al. (2000), Neotectonics of the Min Shan, China: Implications for mechanisms driving Quaternary deformation along the eastern margin of the Tibetan Plateau, *Geological Society of America Bulletin*, *112*, 375-393.

Lease, R. O., et al. (in press), Signatures of mountain building: Detrital zircon U/Pb ages from northeast Tibet, *Geology*.

Li, S., and W. D. Mooney (1998), Crustal structure of China from deep seismic sounding profiles, *Tectonophysics*, *288*, 105-113.

Li, S. L., et al. (2002), A preliminary study on crustal velocity structures of Maqin-Lanzhou-Jingbian deep seismic sounding profile, *Acta Geophysisica Sinica*, *45*, 210-217.

Lippolt, H. J., et al. (1994), (Uranium+thorium)/helium dating of apatite: experience with samples from different geochemical environments, *Chemical Geology*, *112*, 179-191.

Mancktelow, N. S., and B. Grasemann (1997), Time-dependent effects of heat advection and topography on cooling histories during erosion, *Tectonophysics*, *270*, 167-195.

Marrett, R., and P. A. Bentham (1997), Geometric analysis of hybrid fault-propagation/detachment folds, *Journal of Structural Geology*, *19*, 243-248.

Mattauer, M., et al. (1985), Tectonics of the Qinling Belt: Build-up and evolution of eastern Asia, *Nature*, *317*, 496-500.

Métivier, F., et al. (1998), Northeastward growth of the Tibet plateau deduced from balanced reconstructions of two depositional areas: the Qaidam and Hexi Corridor basins, China, *Tectonics*, *17*, 823-842.

Meyer, B., et al. (1998), Crustal thickening in Gansu-Qinghai, lithospheric mantle subduction, and oblique, strike-slip controlled growth of the Tibet plateau, *Geophysical Journal International*, *135*, 1-47.

Ministry of Geology and Mineral Resources, (1989), *Regional Geology of Gansu Province*, 690 pp., Geol. Publishing House, Beijing.

Ministry of Geology and Mineral Resources, (1991), *Regional Geology of Qinghai Province*, 662 pp., Geol. Publishing House, Beijing.

Mitra, S., and J. Namson (1989), Equal-area balancing, *American Journal of Science*, *289*, 563-599.

Molnar, P. (2005), Mio-Pliocene growth of the Tibetan Plateau and evolution of east Asian climate, *Palaeontologia Electronica*, *8*, 2-23.

Molnar, P., et al. (1993), Mantle dynamics, uplift of the Tibetan Plateau, and the Indian monsoon, *Reviews of Geophysics*, *31*, 357-396.

Murphy, M. A., and A. Yin (2003), Structural evolution and sequence of thrusting in the Tethyan fold-thrust belt and Indus-Yalu suture zone, southwest Tibet, *Geological Society of America Bulletin*, *115*, 21-34.

Murphy, M. A., et al. (1997), Did the Indo-Asian collision alone create the Tibetan Plateau?, *Geology*, *25*, 719-722.

Pares, J. M., et al. (2003), Northeastward growth and uplift of the Tibetan Plateau: Magnetostratigraphic insights from the Guide Basin, *Journal of Geophysical Research*, *108*, 2017 (EPM 2011:2011-2011:2011).

Peltzer, G., et al. (1988), Offsets of Late Quaternary morphology, rate of slip, and recurrence of large earthquakes on the Chang Ma fault (Gansu, China), *Journal of Geophysical Research*, *93*, 7793-7812.

Peltzer, G., et al. (1985), Neogene and Quaternary faulting in and along the Qinling Shan, *Nature*, *317*, 500-505.

Reiners, P. W., and K. A. Farley (2001), Influence of crystal size on apatite (U-Th)/He thermochronometry: An example from the Bighorn Mountains, Wyoming, *Earth and Planetary Science Letters*, *188*, 413-420.

Ritts, B. D., et al. (2004), Oligocene-Miocene tectonics and sedimentation along the Altyn Tagh fault, northern Tibetan Plateau: Analysis of the Xorkol, Subei, and Aksay basins, *Journal of Geology*, *112*, 207-229.

Rowley, D. B., and B. S. Currie (2006), Paleo-altimetry of the late Eocene to Miocene Lunpola basin, central Tibet, *Nature*, *439*, 677-681.

Royden, L. (1996), Coupling and decoupling of crust and mantle in convergent orogens: Implications for strain partitioning in the crust, *Journal of Geophysical Research*, *101*, 17,679-617,705.

Royden, L. H., et al. (1997), Surface deformation and lower crustal flow in Eastern Tibet, *Science*, *276*, 788-790.

Schlische, R. W., et al. (1996), Geometry and scaling relations of a population of very small rift-related normal faults, *Geology*, *24*, 683-686.

Schoenbohm, L. M., et al. (2004), Geomorphic constraints on surface uplift, exhumation, and plateau growth in the Red River region, Yunnan Province, China, *Geological Society of America Bulletin*, *116*, 1-15.

Sengör, A. M. C., and B. A. Natal'in (1996), Paleotectonics of Asia: Fragments of a synthesis, in *The Tectonic Evolution of Asia*, edited by A. Yin and T. M. Harrison, pp. 486-641, Cambridge University Press, Cambridge.

Stüwe, K., et al. (1994), The influence of eroding topography on steady-state isotherms. Application to fission track analysis, *Earth and Planetary Science Letters*, *124*, 63-74.

Suppe, J., and D. A. Medwedeff (1990), Geometry and kinematics of fault-propagation folding, *Eclogae Geologicae Helvetiae*, *83*, 409-454.

Tapponnier, P., et al. (1990), Active thrusting and folding in the Qi Lian Shan, and decoupling between the upper crust and mantle in northeastern Tibet, *Earth and Planetary Science Letters*, *97*, 382-403.

Tapponnier, P., et al. (1982), Propagating extrusion tectonics in Asia: New insight from simple experiments with plasticine, *Geology*, *10*, 611-616.

Tapponnier, P., et al. (2001), Oblique stepwise rise and growth of the Tibet Plateau, *Science*, *294*, 1671-1677.

Van der Woerd, J., et al. (2001), Rapid active thrusting along the northwestern range front of the Tanghe Nan Shan (western Gansu, China), *Journal of Geophysical Research*, *106*, 30,475-430,504.

Wolf, R. A., et al. (1998), Modeling of the temperature sensitivity of the apatite (U-Th)/He thermochronometer, *Chemical Geology*, *148*, 105-114.

Wolf, R. A., et al. (1996), Helium diffusion and low-temperature thermochronometry of apatite, *Geochimica et Cosmochimica Acta*, *60*, 4231-4240.

Xu, G., and P. Kamp (2000), Tectonics and denudation adjacent to the Xianshuihe Fault, eastern Tibetan Plateau: Constraints from fission track thermochronology, *Journal of Geophysical Research*, *105*, 19231-19251.

Yin, A., and T. M. Harrison (2000), Geologic evolution of the Himalayan-Tibetan orogen, *Annual Reviews in Earth and Planetary Science*, *28*, 211-280.

Yin, A., et al. (1999), Tertiary deformation history of southeastern and southwestern Tibet during the Indo-Asian collision, *Geological Society of America Bulletin*, *111*, 1644-1664.

Yin, A., et al. (2002), Tectonic history of the Altyn Tagh fault system in northern Tibet inferred from Cenozoic sedimentation, *Geological Society of America Bulletin*, *114*, 1257-1295.

Zeitler, P. K., et al. (1987), U-Th-He dating of apatite: A potential thermochronometer, *Geochimica et Cosmochimica Acta*, *51*, 2865-2868.

Zevenbergen, L. W., and C. R. Throne (1987), Quantitative analysis of land surface topography, *Earth Surface Processes and Landforms*, *12*, 47-56.

Zhang, P.-Z., et al. (2004), Continuous deformation of the Tibetan Plateau from global positioning system data, *Geology*, *32*, 809-812.

Zhao, W. J., and W. J. Morgan (1985), Uplift of Tibetan Plateau, *Tectonics*, *4*, 359-369.

Zheng, D., et al. (2003), Late Cenozoic deformation subsequence in northeastern margin of Tibet - Detrital AFT records from Linxia basin, *Science in China (Series D)*, *46*, 266-275.

Zheng, D., et al. (2006), Rapid exhumation at ~8 Ma on the Liupan Shan thrust fault from apatite fission-track thermochronology, *Earth and Planetary Science Letters*, *248*, 183-193.

Zhou, D., and S. A. Graham (1996), Songpan-Ganzi complex of the west Qilian Shan as a Triassic remnant ocean basin, in *The Tectonic Evolution of Asia*, edited by A. Yin and T. M. Harrison, pp. 281-299, Cambridge University Press, Cambridge.

Table 1. Geometry of the West Qinling fault

Location	Lat (°N)	Lon (°E)	Strike[a]	Dip[a]	Strike[b]	Dip[b]
Eastern fault tip	35.152	103.614	168°	38° SW	162°	26° SW
Between Daxia/Tao Rivers	35.231	103.481	93°	42° SW	96°	38° SW
Near Daxia River	35.285	103.254	95°	48° SW	118°	28° SW

[a] Geometry determined from *[Ministry of Geology and Mineral Resources, 1989]*

[b] Geometry determined using SRTM topographic data as base

Table 2. (U-Th)/He data

Sample	[U] (ppm)	[Th] (ppm)	[^{4}He] (nmol/g)	Half-width[a] (μm)	Length (μm)	F_T[b]	Raw Age (Ma)	Corr. Age[c] (Ma)	Uncertainty[d] (m.y.)
CA-04-3: 35.22115°N, 103.28287°E (3650m)									
CA-04-3A	55.2	151	20.3	57	240	0.75	41.2	54.7	3.3
CA-04-3B[e]	16.9	38.6	5.79	57	309	0.76	40.8	53.5	3.2
CA-04-3C	35.3	62.3	10.8	57	240	0.76	39.6	52.4	3.1
CA-04-3D	34.7	81.8	12.1	63	274	0.78	41.2	53.1	3.2
Mean	**41.7**	**98.2**	**14.4**	**59**	**251**	**0.76**	**40.7**	**53.4**	**1.2**
CA-05-2: 35.22115°N, 103.28287°E (3650m)									
CA-05-2A[e]	38.0	93.2	12.9	51	206	0.72	39.3	54.2	3.3
CA-05-2B	64.9	115	20.6	50	287	0.74	40.9	55.6	3.3
CA-05-2C	43.3	102	15.2	47	291	0.72	41.3	57.3	3.4
CA-05-2D	54.4	112	16.4	51	273	0.74	37.2	50.5	3.0
Mean	**54.2**	**110**	**17.4**	**49**	**284**	**0.73**	**39.8**	**54.4**	**3.5**
CA-04-4: 35.21613°N, 103.28982°E (3507m)									
CA-04-4A	43.0	98.5	16.6	51	206	0.73	46.1	63.4	3.8
CA-04-4B	41.1	94.0	12.5	57	309	0.76	36.2	47.4	2.8
CA-04-4C	68.9	113	15.5	51	257	0.74	29.8	40.4	2.4
CA-04-4D	40.3	63.1	7.42	57	240	0.76	24.7	32.6	2.0
Mean	**48.3**	**92.0**	**13.0**	**54**	**253**	**0.75**	**34.2**	**46.0**	**13**
CA-04-5: 35.21428°N, 103.29602°E (3400m)									
CA-04-5A	36.8	104	9.61	51	223	0.73	28.9	39.6	2.4
CA-04-5B	42.4	127	9.49	51	326	0.74	24.1	32.5	1.9
CA-04-5D	69.2	145	10.3	51	171	0.72	18.2	25.4	1.5
CA-04-5E	40.1	70.2	6.89	40	189	0.67	22.4	33.5	2.0
Mean	**47.1**	**111**	**9.07**	**48**	**227**	**0.71**	**23.4**	**32.7**	**5.8**
CA-04-6: 35.20833°N, 103.29602°E (3319m)									
CA-04-6A	61.5	56.6	10.5	86	240	0.82	25.8	31.4	1.9
CA-04-6B	43.4	121	9.05	80	360	0.82	23.1	28.1	1.7
CA-04-6C	49.9	64.7	12.5	86	360	0.83	35.2	42.1	2.5
Mean	**51.6**	**80.8**	**10.7**	**84**	**320**	**0.83**	**28.0**	**33.9**	**7.3**
CA-04-8: 35.20828°N, 103.30522°E (3085m)									
CA-04-8A	58.8	115	8.16	57	343	0.77	17.5	22.8	1.4
CA-04-8B	79.5	139	10.9	63	411	0.79	17.8	22.6	1.4
CA-04-8C	52.2	93.1	7.38	57	274	0.76	18.3	24.1	1.4
CA-04-8D	45.9	84.8	5.48	57	257	0.76	15.3	20.2	1.2
CA-04-8E	39.1	125	6.77	57	257	0.75	18.1	24.1	1.4
CA-04-8F	48.0	86.2	6.22	51	257	0.74	16.7	22.7	1.4
CA-04-8G	42.3	122	7.88	51	274	0.74	20.4	27.7	1.7
CA-04-8H	46.5	91.9	9.14	57	189	0.74	24.7	33.1	2.0
Mean	**51.5**	**107**	**7.74**	**56**	**283**	**0.75**	**18.6**	**24.7**	**4.0**
CA-05-4: 35.21381°N, 103.30780°E (3039m)									
CA-05-4A	34.5	92.4	3.85	49	202	0.71	12.5	17.6	1.1
CA-05-4B	36.4	96.0	4.13	42	200	0.68	12.8	18.9	1.1
CA-05-4C	33.8	95.7	3.26	48	270	0.72	10.6	14.7	0.9
CA-05-4D[e]	40.2	131	6.32	48	235	0.72	16.3	22.8	1.4
Mean	**34.9**	**94.7**	**3.75**	**46**	**224**	**0.70**	**12.0**	**17.0**	**2.1**

CA-04-9: 35.21980°N, 103.31092°E (2967m)									
CA-04-9A	94.5	76.7	6.62	46	377	0.73	10.8	14.8	0.9
CA-04-9B	150	145	33.6	57	257	0.76	33.5	44.0	2.6
CA-04-9C	159	146	38.0	51	257	0.74	35.9	48.4	2.9
CA-04-9D	124	106	29.8	57	326	0.77	36.7	47.7	2.9
CA-04-9E	148	114	26.3	69	206	0.78	27.6	35.2	2.1
CA-04-9F	115	64.8	17.6	57	291	0.77	24.8	32.3	1.9
CA-04-9G	93.3	99.4	11.5	74	411	0.82	18.1	22.1	1.3
Mean	**126**	**107**	**23.3**	**59**	**304**	**0.77**	**26.8**	**34.9**	**13**
CA-05-5: 35.21980°N, 103.31092°E (2967m)									
CA-05-5A	90.8	78.9	8.62	57	259	0.76	14.4	18.9	1.1
CA-05-5B[e]	175	152	37.0	49	194	0.72	32.2	44.6	2.7
CA-05-5C	172	149	14.5	54	256	0.75	12.9	17.2	1.0
CA-05-5D	177	132	22.4	51	185	0.73	19.8	27.2	1.6
Mean	**146**	**120**	**15.2**	**54**	**233**	**0.75**	**15.7**	**21.1**	**5.4**
CA-04-10: 35.23417°N, 103.35262°E (2602m)									
CA-04-10A	15.2	55.7	2.63	57	309	0.76	17.1	22.5	1.3
CA-04-10B	19.3	61.1	1.92	40	240	0.67	10.5	15.6	0.9
CA-04-10C	23.8	25.8	4.26	57	291	0.77	26.2	34.2	2.1
CA-04-10D	25.5	35.2	3.97	57	257	0.76	21.6	28.4	1.7
CA-04-10E	15.7	43.9	2.83	51	291	0.74	20.0	27.1	1.6
CA-04-10F	16.9	65.8	2.55	46	189	0.69	14.4	20.8	1.3
Mean	**19.4**	**47.9**	**3.03**	**51**	**263**	**0.73**	**18.3**	**24.8**	**6.5**

[a] Measured half-with of prism.

[b] Alpha retentivity for a hexagonal prism (Farley et al. 1996)

[c] Age corrected for alpha ejection, following Farley et al. (1996)

[d] Uncertainties on single replicates are 6% (2σ) and represent typical laboratory reproducibility (Farley, 2002). Uncertainties on sample mean ages are taken as the standard deviation (2σ) of the mean.

[e] Replicates excluded from sample mean calculations because of He release upon reheating.

Table 3. Estimates of shortening and crustal thickness

Model	Minimum (km)	Maximum (km)
TAO HE TIP-LINE ANTICLINE		
Shallow, subhorizontal décollement	1.0 (8%)	1.8 (14%)
Shallow, subhorizontal décollement (including southwestern anticline)	1.4 (7%)	2.1 (11%)
Hybrid fault-propagation/detachment fold	0.8 (7%)	1.1 (9%)
Tri-shear with horizontal décollement	2.4 (20%)	3.0 (24%)
Tri-shear with dipping detachment	1.5 (11%)	1.9 (15%)
LINTAN BASIN MARGIN		
Tri-shear with horizontal décollement	2.4 (11%)	6.5 (31%)
Tri-shear with dipping detachment	1.0 (5%)	N/A
TOTAL SHORTENING[a]		
Tri-shear with horizontal décollement	5.2 (10%)	9.9 (17%)
Tri-shear with dipping detachment	2.9 (6%)	3.3 (7%)

[a]Sum of shortening estimates on Linxia and Lintan basin margins

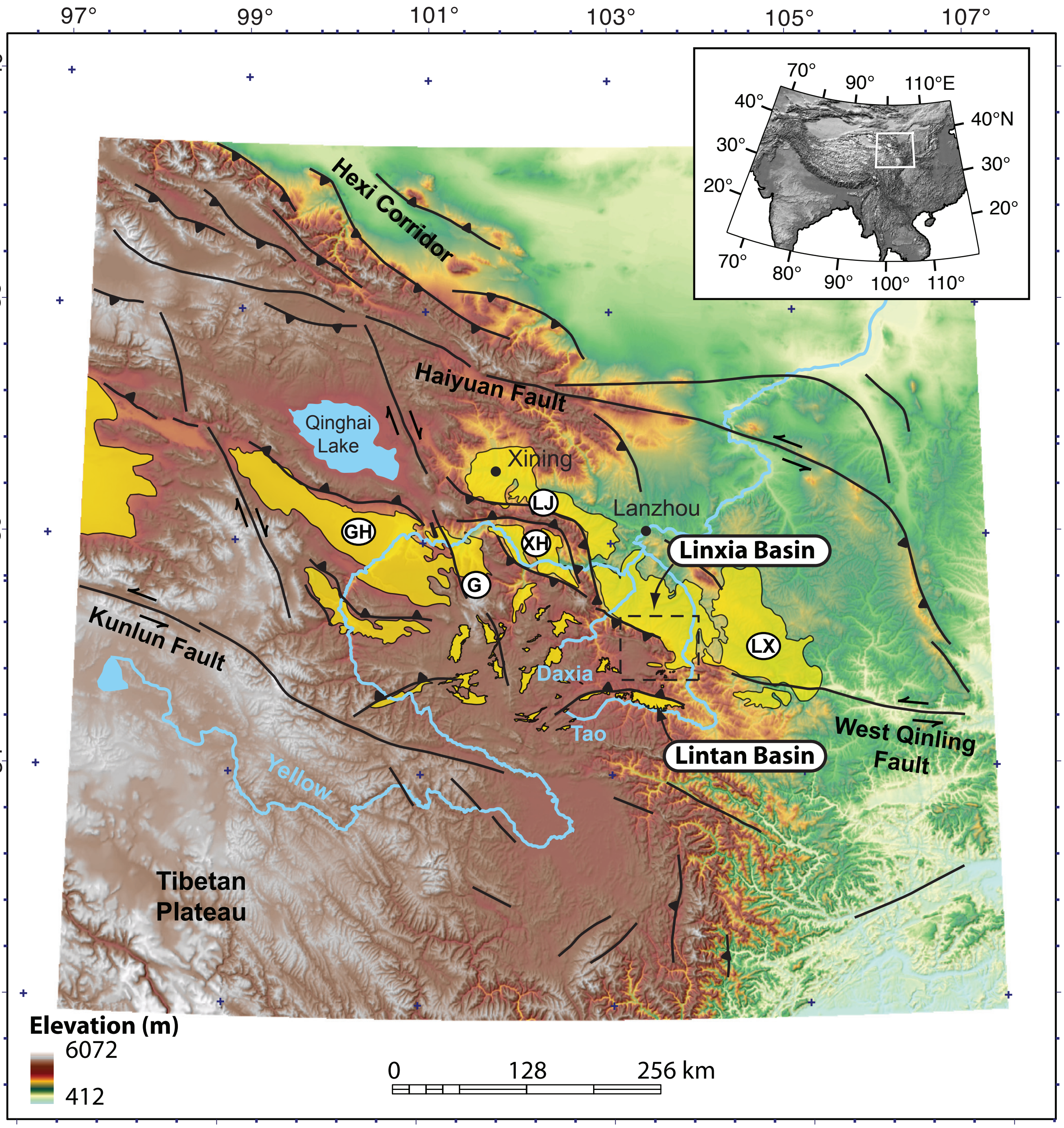

Angerman et al., Deformation in NE Tibet - Figure 1

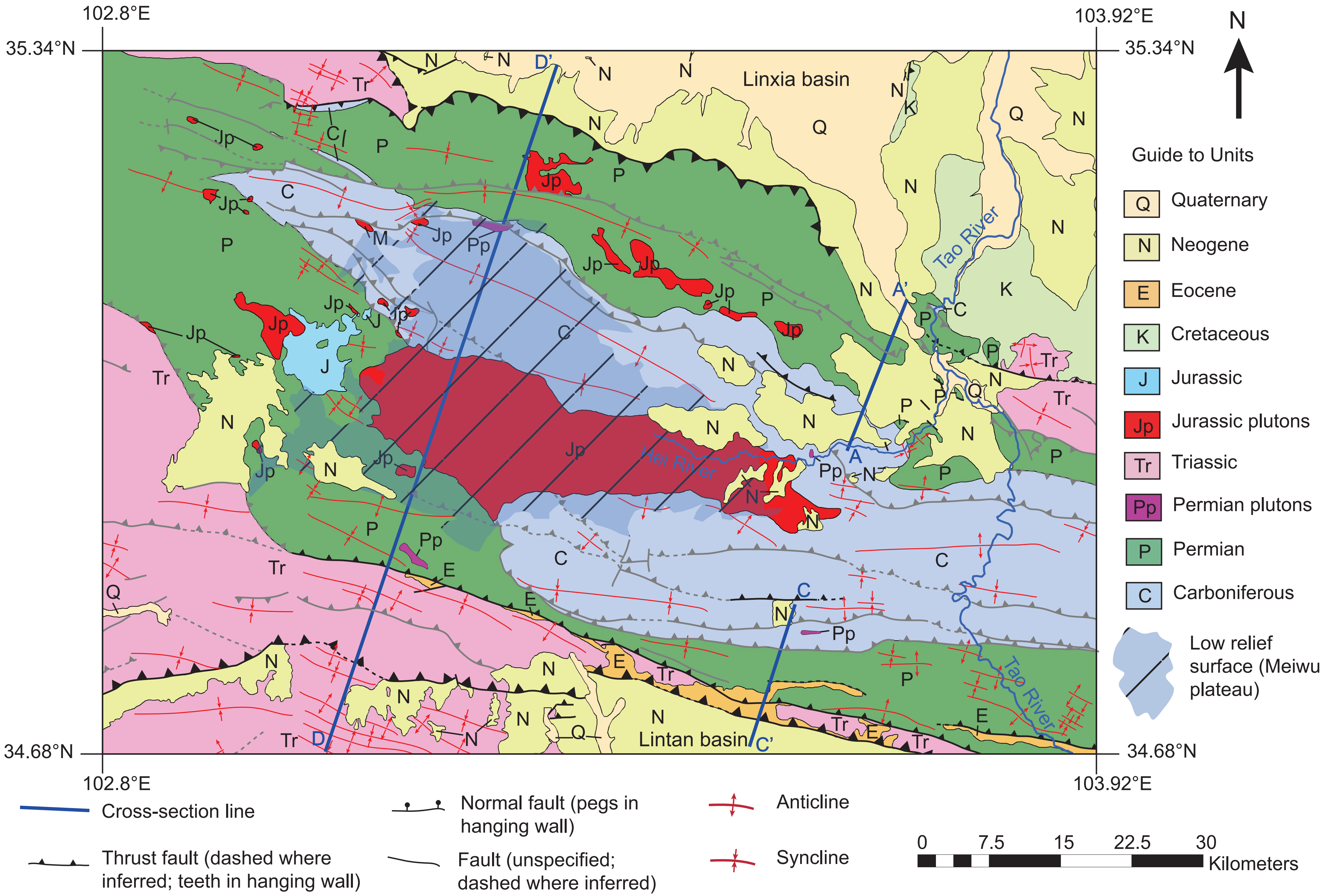

Angerman et al., Deformation in NE Tibet - Figure 2

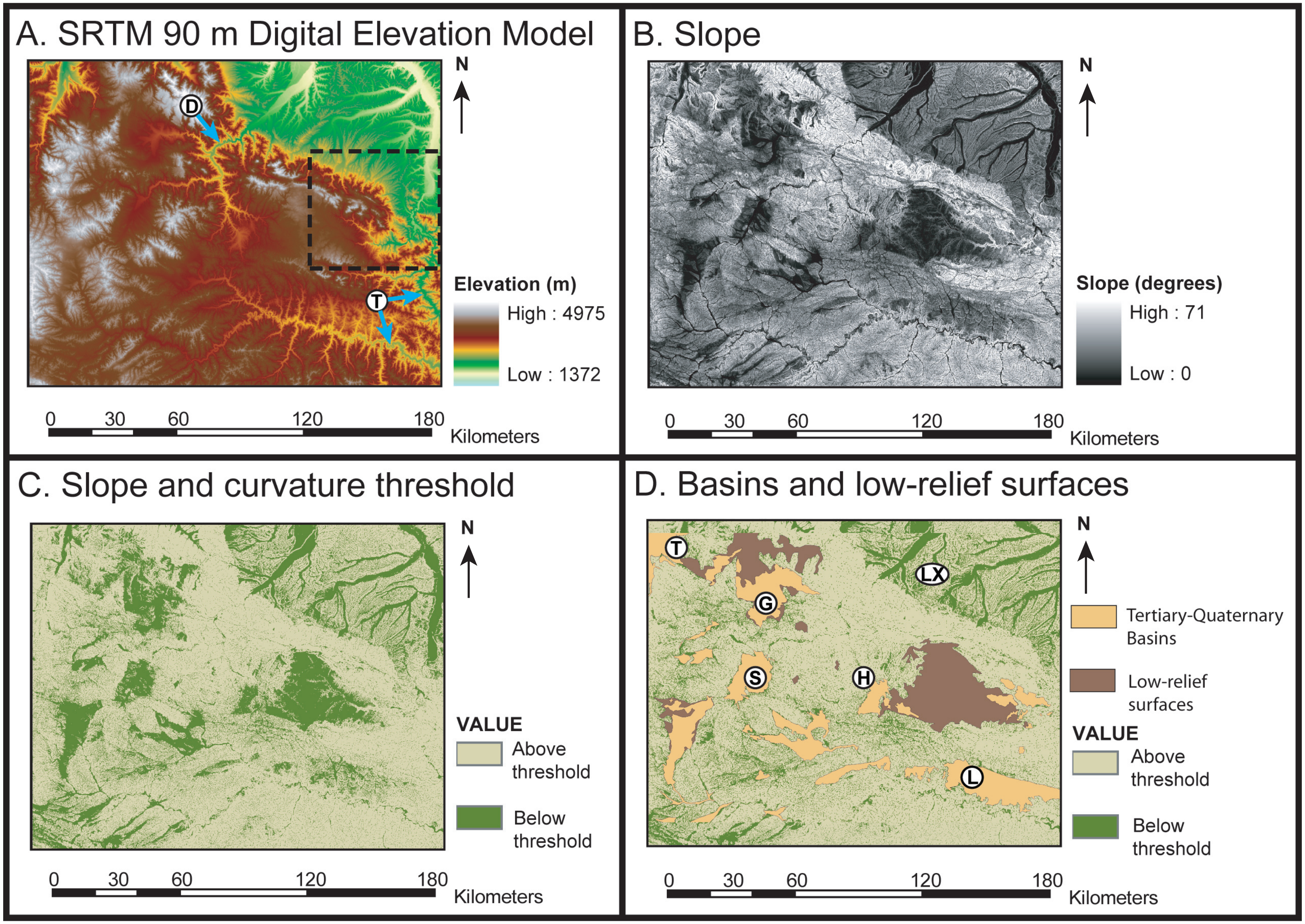

Angerman et al., Deformation in NE Tibet - Figure 3

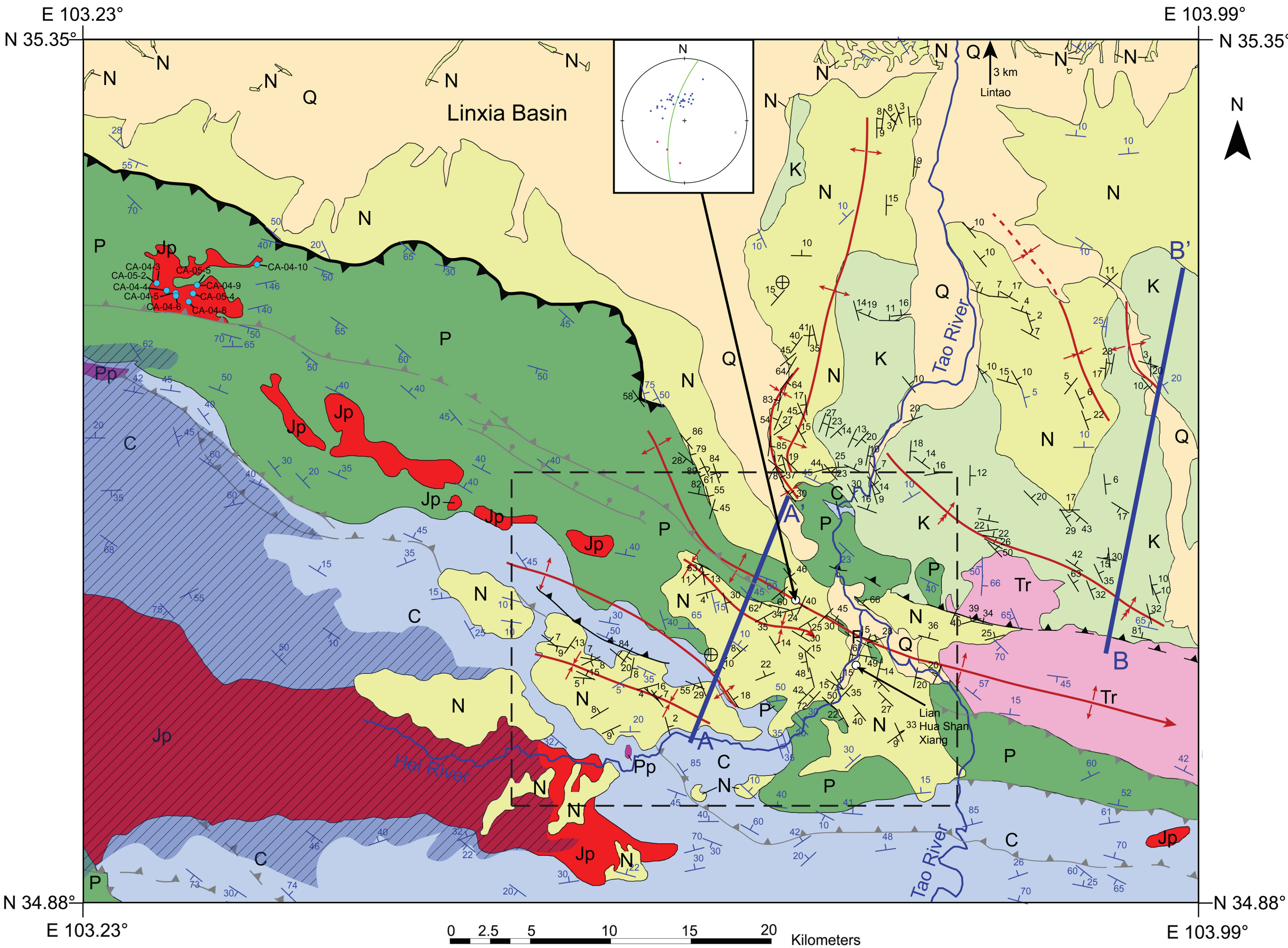

Angerman et al., Deformation in NE Tibet - Figure 4

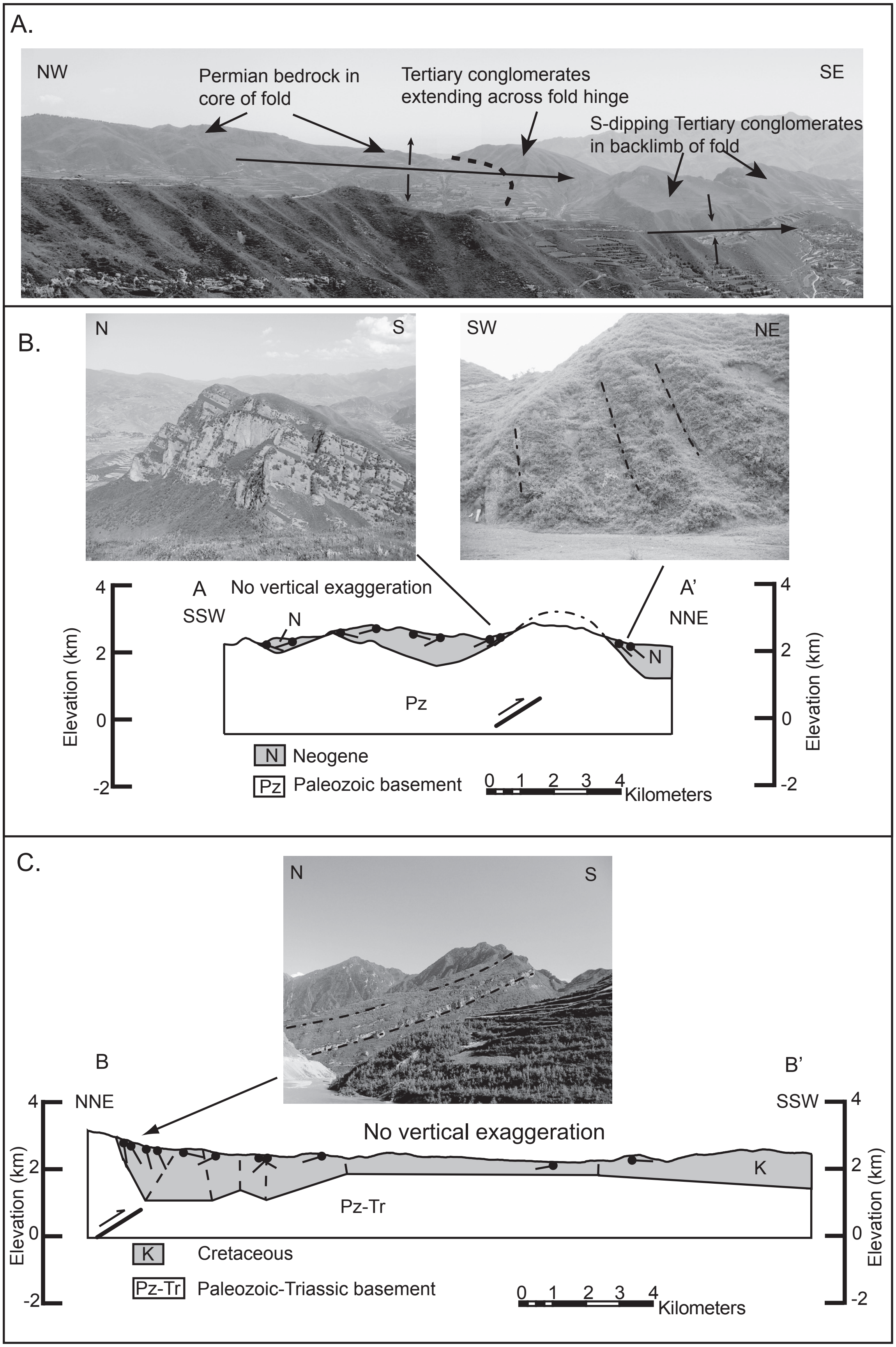

Angerman et al., Deformation in NE Tibet - Figure 5

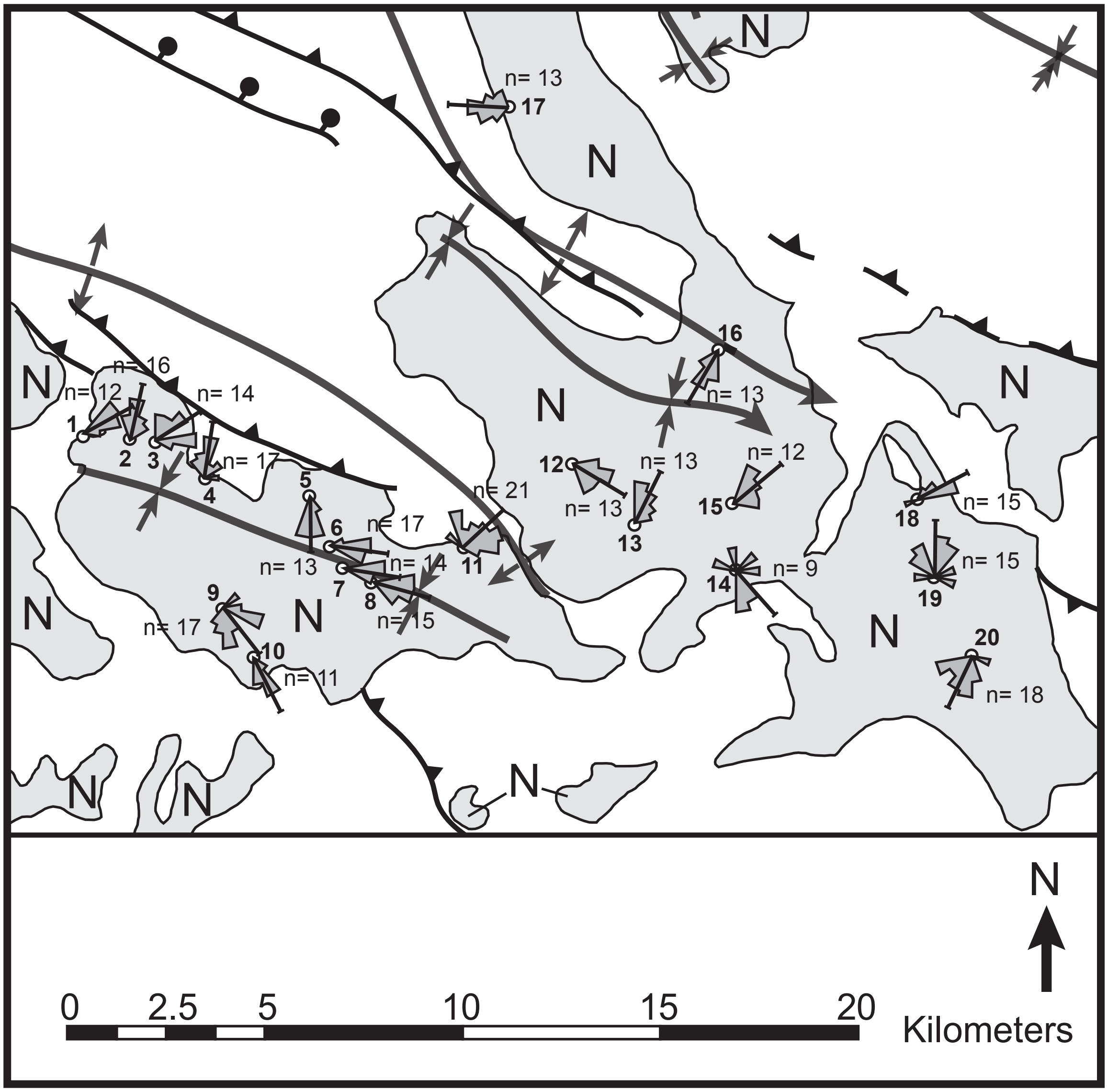

Angerman et al., Deformation in NE Tibet - Figure 6

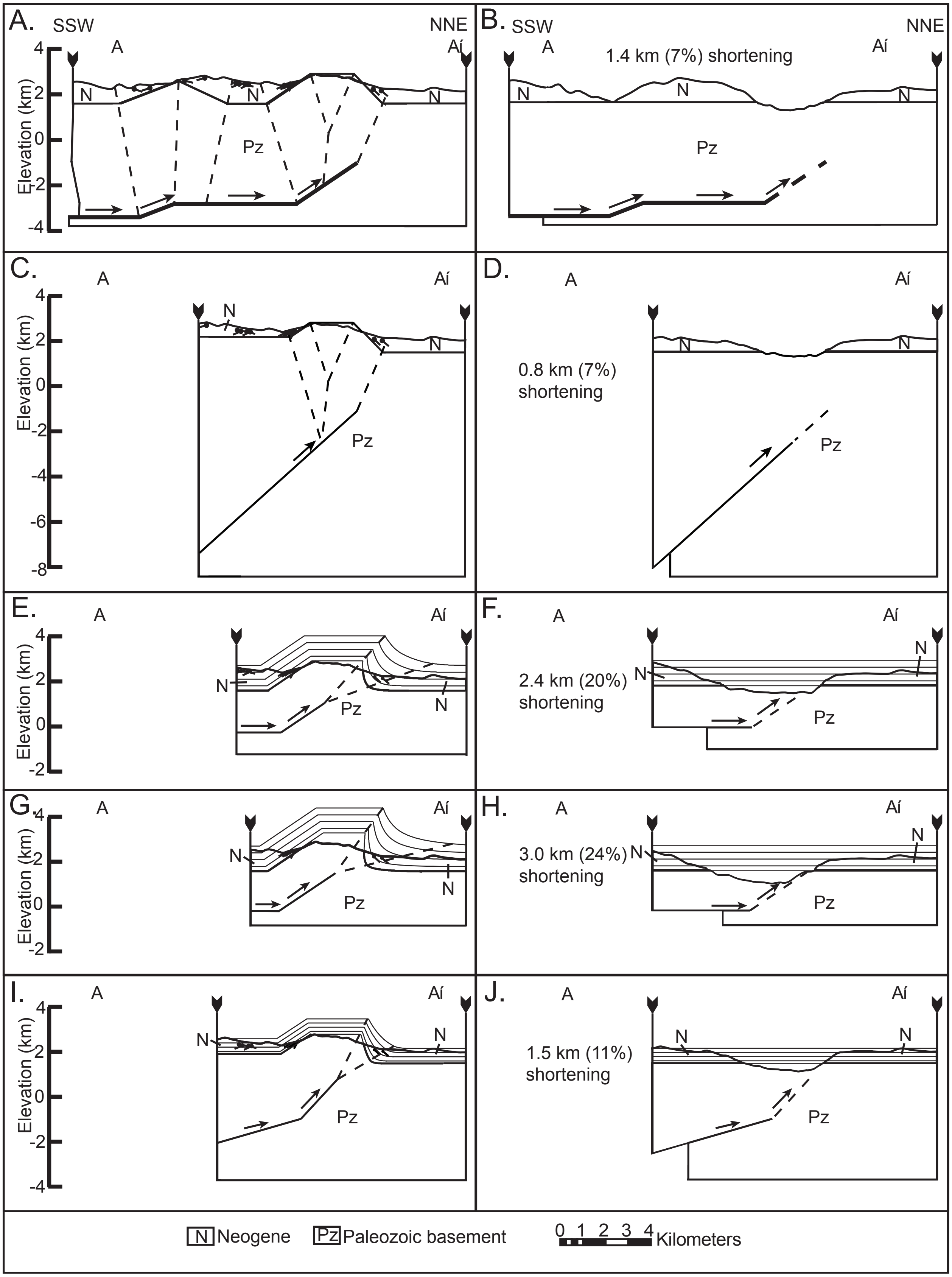

Angerman et al., Deformation in NE Tibet - Figure 7

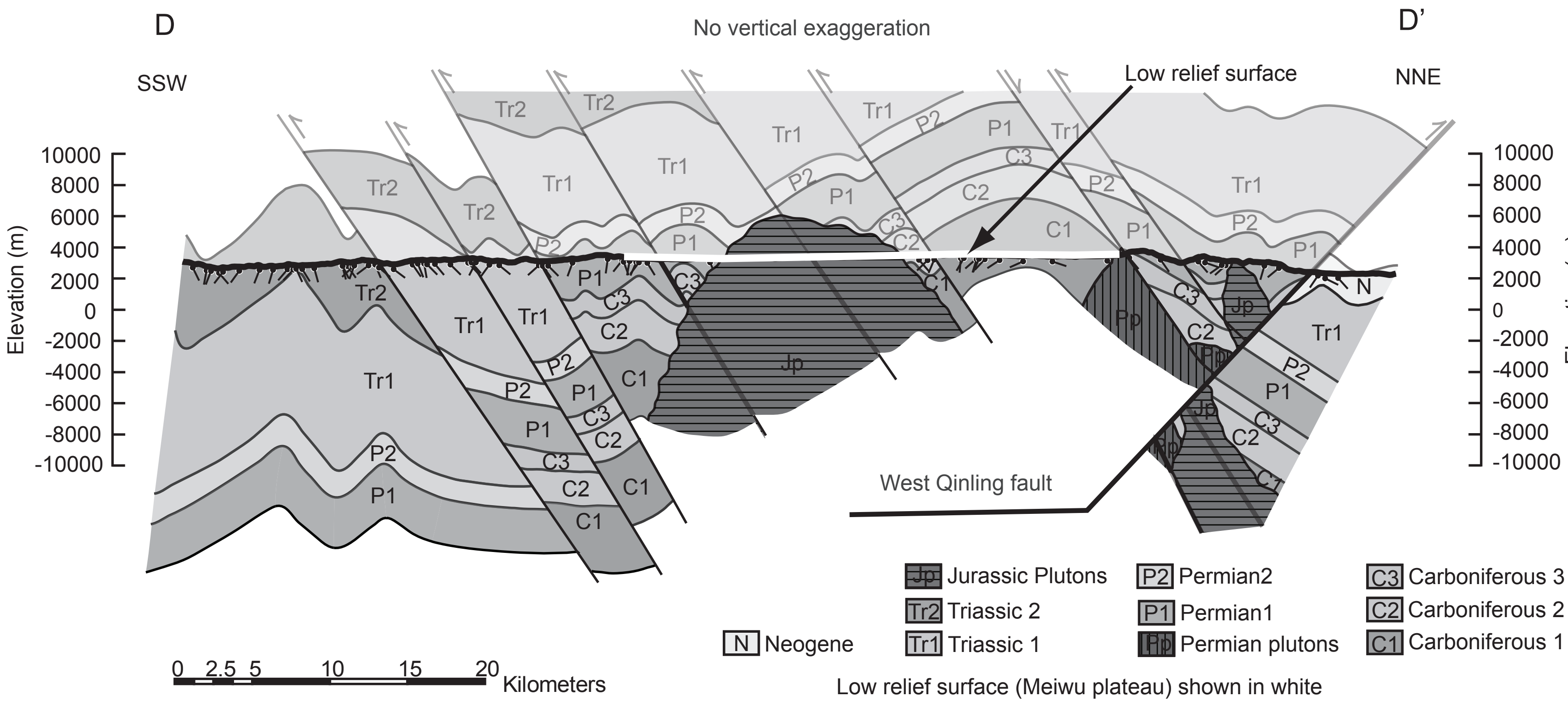

Angerman et al., Deformation in NE Tibet - Figure 8

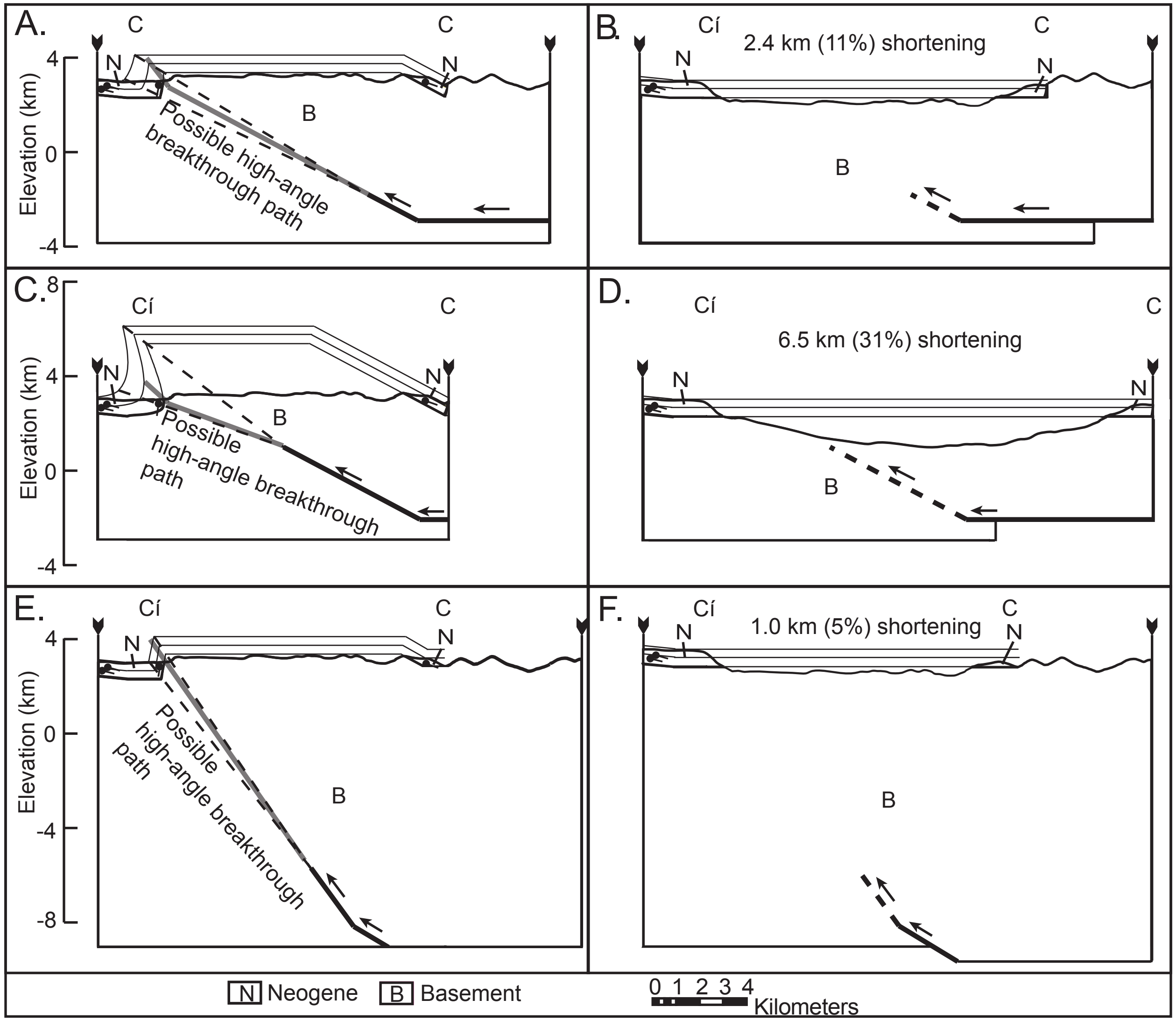

Angerman et al., Deformation in NE Tibet - Figure 9

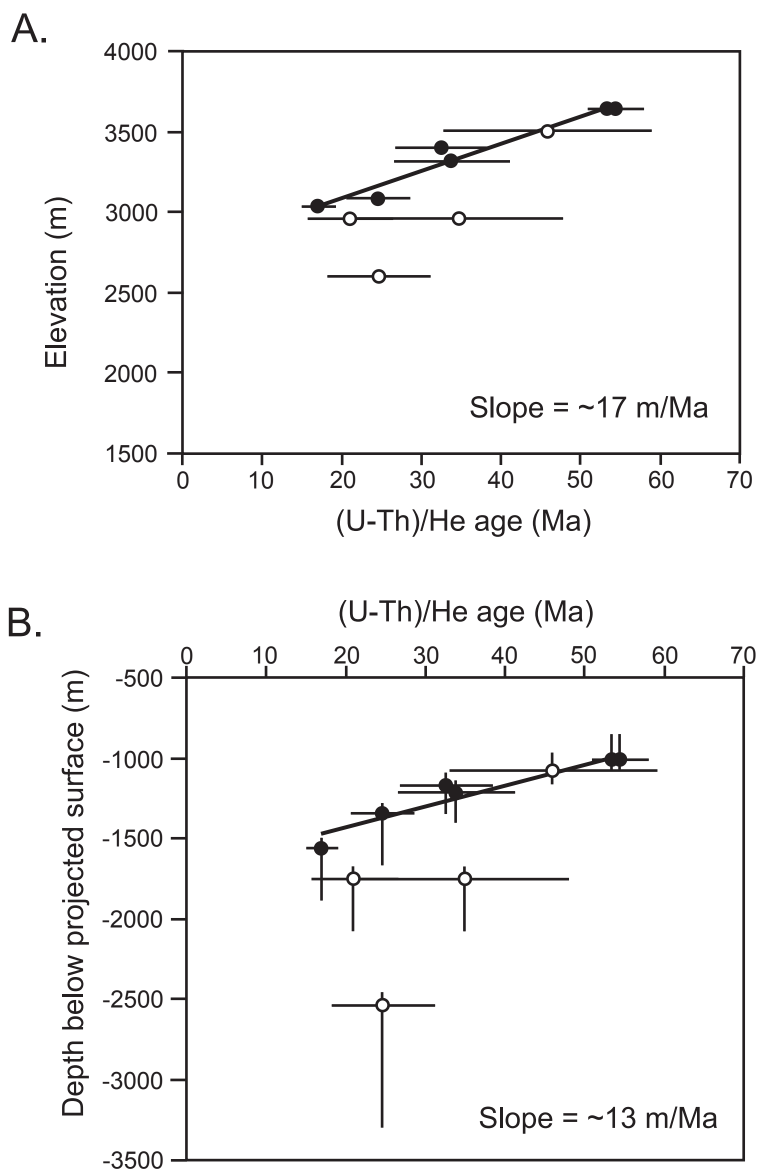

Angerman et al., Deformation in NE Tibet - Figure 10